Dissertation

submitted to the

Combined Faculties of the Natural Sciences and Mathematics

of the Ruperto-Carola-University of Heidelberg, Germany

for the degree of

Doctor of Natural Sciences

Put forward by

Renato Ferracini Alves

Born in: Jundiaí, São Paulo, Brazil

Oral examination: February 2nd, 2022

Realization of a Heisenberg XXZ spin system using Rydberg atoms

Referees: **Prof. Dr. Matthias Weidemüller**

Prof. Dr. Jörg Evers

Abstract

In this thesis we present the realization of an isolated Heisenberg XXZ spin 1/2 system with off-diagonal disorder in the coupling constants using cold atoms in highly excited Rydberg states. We select a set of Rydberg states that interact via van der Waals interaction which can be mapped onto an interacting spin system. We investigate the out-of-equilibrium dynamics of the spin system after it has been initialized in a fully magnetized state. Following unitary evolution governed by the Heisenberg spin Hamiltonian we measure the magnetization as function of the evolution time. By fitting a stretched exponential function to the resulting magnetization dynamics be obtain a stretched exponent of $\beta = 0.32$ revealing a slow relaxation of the spin system, similar to what is found in spin-glasses. By choice, the initial state is an eigenstate of the mean field Hamiltonian and thus the observed relaxation indicates that the dynamics is triggered by quantum fluctuations. We find that varying the distribution of coupling constants by means of the so-called dipole blockade effect has no impact on the stretching exponent indicating that it is an universal parameter of the system independent of the microscopic details for the range of disorder explored in the experiment. It also allows us to combine the different datasets by re-scaling the time domain with the characteristic interaction strength. The combined datasets expands our measurements to two orders of magnitude in the re-scaled time domain showing that slow dynamics is a persistent effect for long evolution times.

Zusammenfassung

Diese Arbeit beschreibt die Realisierung eines isolierten Heisenberg XXZ Spin-1/2-Systems mit nichtdiagonaler Unordnung in den Kopplungskonstanten mittels kalten Atomen in hoch angeregten Rydberg Zuständen. Wir verwenden einen Satz von Rydberg Zuständen, die über Van-der-Waals-Wechselwirkung wechselwirken, welche auf ein wechselwirkendes Spinsystem abgebildet werden können. Wir untersuchen die Nicht-Gleichgewichts-Dynamik des Spinsystems, nachdem es in einem vollständig magnetisierten Zustand initialisiert wurde. Nach unitärer Evolution, die durch den Heisenberg Spin Hamiltonian bestimmt ist, messen wir die Magnetisierung als Funktion der Evolutionszeit. Durch Anpassen einer *streched exponential* Funktion an die resultierende Magnetisierungsdynamik erhält man einen *streched exponent* von $\beta = 0,32$, der eine langsame Relaxation des Spinsystems anzeigt, ähnlich wie bei Spingläsern. Beabsichtigter Weise ist der Anfangszustand ein Eigenzustand des *mean field* Hamiltonians und somit zeigt die beobachtete Relaxation an, dass die Dynamik durch Quantenfluktuationen ausgelöst wird. Wir finden, dass die Veränderung der Verteilung der Kopplungskonstanten mittels des sogenannten Dipolblockadeeffekts keinen Einfluss auf den streched exponent hat. Dies deutet darauf hindeutet, dass es sich um einen universellen Parameter des Systems handelt, der unabhängig von den mikroskopischen Details ist für den Bereich der Unordnung, der im Experiment untersucht wurde. Es ermöglicht uns auch, die verschiedenen Datensätze zu kombinieren, indem wir die Zeitachse mit der charakteristischen Wechselwirkungsstärke neu skalieren. Die kombinierten Datensätze erweitern unsere Messungen auf zwei Größenordnungen im neu skalierten Zeitbereich und zeigen, dass langsame Dynamik ein anhaltender Effekt für lange Evolutionszeiten ist.

Contents

Introduction

Chapter 1

Contents

Understanding the emergent properties of many particles is an ongoing challenge in physics. To explain the meaning of emergent property we can use an example from classical statistical mechanics: the pressure of a gas. Even though Newton's laws of motion for a single particle where known, it took 180 years for James Clark Maxwell to give it a microscopic description [Coleman, 2015]. To know laws and emergent principles arises when we go from the quantum description of a few particles to a macroscopic system is the goal of many-body physics [Anderson, 2008], a broad field that includes, for example, most of solid state physics. Some of its notable achievements are the Bardeen-Cooper-Schrieffer theory of superconductivity [Bardeen, Cooper, and Schrieffer, 1957], and the description of superfluidity [Landau, 1941].

From the different open questions in many-body physics, we are interested in how an isolated quantum system relaxes. The current understanding is that if the system reaches a thermal state it does so by building up entanglement, such that a part of the whole is sufficiently entangled with the rest of ensemble [Ueda, 2020]. One known mechanism through which thermalization occurs in isolated-many-body systems is the eigenstate thermalization hypothesis (ETH). According to ETH for certain conditions of the many-body spectrum and occupation numbers the diagonal ensemble resembles that of a micro-canonical ensemble. This means that every eigenstate of the Hamiltonian implicitly contains a thermal state initially hidden by the coherence between the eigenstates, but time dynamics reveals it through dephasing [Rigol, Dunjko, and Olshanii, 2008].

The scope of this thesis will be limited to the dynamics of an isolated and disordered many-body spin system. Spins are a prototypical model for many-body physics because they are conceptually simple, but from the interplay of these simple particles many interesting and non-trivial physical properties appear [Parkinson and Farnell, 2010]. They often have quantum phase transitions, and are a canonical model for the study of of these phenomena [Sachdev, 2017]. Furthermore, they are also have application in quantum computing [Glaetzle et al., 2017] where it

has been shown that Ising spin glass Hamiltonian can be mapped into different NP problems [Lucas, 2014; Venturelli et al., 2015].

Investigating many-body systems by means of calculation with classical computers is an extremely difficult task, because the Hilbert space grows exponentially with the number of particles, which makes even current super-computers able to calculate only up to 50 particles. In 3D such system would still be subject to strong finite size effects. Richard Feynman described this problem in his famous 1982 paper "Simulating physics with computers", and his proposed idea to simulate a quantum many-body would be to used another, well controlled, synthetic quantum system [Feynman, 1982]. At the time of this proposal, there was no technology available to accomplish that idea, but today there are a few platforms that achieve the degree of precision and control necessary to realize a synthetic quantum simulator [Altman et al., 2021]. To name a few platforms that can simulate a many-body spin system, there are: superconducting quantum computers [Smith et al., 2019], NV centers [J. Choi et al., 2017], laser cooled and trapped ions [Monroe et al., 2021; Lanyon et al., 2017; Kaplan et al., 2020], ultracold neutral atoms in optical lattices [Bloch, Dalibard, and Nascimbène, 2012], ultracold magnetic atoms [Paz et al., 2013; Tang et al., 2018], cold and ultracold molecules [Bilitewski et al., 2021; Bohn, A. M. Rey, and Ye, 2017], and finally cold Rydberg atoms [Browaeys and Lahaye, 2020].

Our platform of choice to study the dynamics of spins is cold Rydberg atoms. A recent and successful approach to simulation of spins with Rydberg atoms is to use optical lattices and tweezers to achieve local control of each spin [Labuhn et al., 2016; Barredo, Léséleuc, et al., 2016; Endres et al., 2016; Zeiher, Bijnen, et al., 2016]. A few of its achievements are observation of crystallization of excitations [Schauß et al., 2015], exploration of quench dynamics where long-lived oscillations of a antiferromagnetic state were measured [Bernien et al., 2017] and observation of collapse and revival of magnetization in an array of atoms suddenly subjected to Ising interaction by Rydberg dressing [Zeiher, J.-y. Choi, et al., 2017], and extraction of the critical exponent of a quantum phase transition [Keesling et al., 2019].

Our approach to Rydberg spin simulation is rather different. We create a 3D system with on the order of a thousand spins which are distributed randomly. We initially prepare the spins in a full magnetized and out-off-equilibrium state, and let they evolve under unitary dynamics unitary dynamics of a Heisenberg XXZ Hamiltonian.

In this thesis we will present the relaxation of the magnetization in this out-of-equilibrium isolated system, which is the main our main contribution to the field of simulated spin systems.

1.1 Outline

Starting with chapter 2, we will focus on Rydberg atoms properties and how their long range interaction can be mapped to different spin systems, depending on the choice of Rydberg states. Chapter 3 introduces the experimental platform used to realize the Rydberg spin systems, and shows how we excite, manipulate and detect Rydberg spins. In chapter 4 we present the measurement of the magnetization relaxation of a Heisenberg XXZ spin system. Finally, we make a conclusion of this thesis work in chapter 5.

Chapter 2

Interacting Rydberg atoms mapping to Heisenberg XXZ spins

Contents

This chapter is partially based on the following publications, from which parts of the text are reproduced verbatim:

Glassy Dynamics in a Disordered Heisenberg Quantum Spin System A. Signoles, T. Franz, R. Ferracini Alves, M. Gärttner, S. Whitlock, G. Zürn, M. Weidemüller. Physical Review X, Vol. 11, No. 1 (2021)

The author contributed to the experimental apparatus, data acquisition and analysis, and a algorithm to generate the initial spin distribution for the dTWA simulations.

Depletion imaging of Rydberg atoms in cold atomic gases M. Ferreira-Cao, V. Gavryusev, T. Franz, R. Ferracini Alves, A. Signoles, G. Zürn, M. Weidemüller. J. Phys. B, Vol. 53, No. 8 (2020)

The author contributed with experimental setup, data acquisition and analysis, simulation of the initial spin distribution, and on the interpretation of the results.

2.1 Introduction

This chapter presents how the long-range Rydberg interactions can be used to used to simulate spin systems in ultracold gases. We start by a general description of a Rydberg atom, and proceed by showing how their exaggerated properties, in particular the large dipole moment, leads to long-range dipolar and van der Waals interactions. Finally, we show that Rydberg interactions can be mapped into spin 1/2 systems, if we can truncate the internal degrees of freedom into only two states of the Hilbert space. In particular we show the mapping for three different spin 1/2 systems: Ising, XX, and XXZ.

property	notation	scaling α in $(n^*)^\alpha$
orbital radius	$\langle r \rangle$	2
binding energy	E_n	-2
level separation	$E_{n+1} - E_n$	-3
ionization field	ϵ	-4
polarizability	α	7
radiative lifetime	τ_r	3
black body lifetime	τ_{BB}	2
dipolar interaction	C_3	4
van der Waals interaction	C_6	11

Tab. 2.1 Selected scaling properties of Rydberg atoms with respect to the effective principal quantum number n^* [Gallagher, 1994].

2.2 Alkali Rydberg atoms

Atoms excited to high-lying atomic states with large principal quantum number n are called Rydberg atoms. In these states, the electron is weakly bound and the orbital radius, scaling with n^2, can be hundreds of times larger than the ground state. When exciting alkali atoms to Rydberg states, because the valence electron is on average far from the nucleus, the electronic inner shells shield the nuclear charges from the valence electron, making it experience an effective core charge of $Z = 1$. In this approximation, the valence electron experiences an hydrogen-like potential, and the wave functions of alkali Rydberg atoms resembles that of hydrogen. Nevertheless, for states with low orbital angular momentum $\ell < 3$ the electron has a finite probability of penetrating the core, leading to a correction in binding energy and lifting the ℓ-degeneracy. This correction also causes a phase shift of the wave function with respect to hydrogen wave functions.

Many important properties of Rydberg atoms scale with powers of the effective principal quantum number. Some of these scaling properties are summarized in table 2.1.

2.2.1 Rydberg spectrum

Janne Rydberg found in 1888 an empirical equation $E = -\mathrm{R} \,/\, n^2$, that predicted the Hydrogen energy spectrum. Here E corresponds to the binding energy of the electron, n is the principal quantum number, and R the Rydberg constant. Even though it is a generalization of the Balmer

formula, created three years before, his work is considered independent and demonstrated a great achievement of unveiling a simple pattern out of a apparently complex numerical data. With the Bohr atomic theory, and later the quantum mechanics, it was possible to deduce the Rydberg constant from other more fundamental quantities,

$$\mathrm{R} = \frac{e^4 m_e}{16\pi^2 \epsilon_0^2 \hbar^2} \times \frac{m_a}{m_a + m_e} = \mathrm{R}_\infty \times \frac{m_a}{m_a + m_e} \tag{2.1}$$

where e and m_e are the electron charge and mass, ϵ_0 the electrical vacuum permittivity, $\hbar$ the reduced Planck constant, and m_a the atomic mass [Martinson and Curtis, 2005]. The fundamental Rydberg constant is $\mathrm{R}_\infty = 109737.315\, cm^{-1}$ [Sansonetti, 2003], without accounting for the reduced mass. As and example, the ^{87}Rb Rydberg constant, with the reduced mass correction, is $\mathrm{R}_{Rb} = 109736.605\, cm^{-1}$ [Li et al., 2003].

In order to extend the Rydberg formula to heavier Alkali atoms, the quantum defect theory is used [Seaton, 1983; Rau and Inokuti, 1997]. It models the imperfect shielding of the nuclear charges by the inner electrons by modifying the principal quantum number, which leads to the modified Rydberg equation

$$E_{n\ell j} = -\frac{\mathrm{R}}{(n - \delta_{n\ell j})^2} = -\frac{\mathrm{R}}{(n^*)^2} \tag{2.2}$$

where the principal quantum number n is subtracted by the quantum defect $\delta_{n\ell j}$ factor. Note that $\delta_{n\ell j}$ depends on the principal quantum number n, and on the orbital and total angular momentum, ℓ and j respectively. Here we also define $n^* = (n - \delta_{n\ell j})$ as the effective principal quantum number.

The spectrum given by the quantum defect theory is depicted in figure 2.2. Figure 2.1 (a) shows that the quantum defect asymptotically converges to a constant value with increasing principal quantum number, and figure 2.1 (b) shows that the quantum defect approaches zero with increasing azimuthal quantum number. The quantum defects are of empirical nature, and are determined by measurements of atomic spectrum [Li et al., 2003].

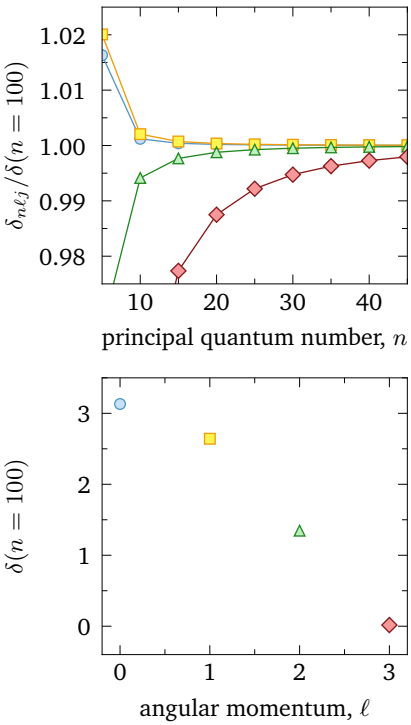

Fig. 2.1 Quantum defect. The top figure shows quantum defects for rubidium-87 as a function function of principal quantum number n. We show values for different orbital angular momentum (blue, $\ell = 0$; yellow, $\ell = 1$, green, $\ell = 2$, red, $\ell = 3$) . The values are normalize to $n = 100$ in order to show the asymptotic behavior for large n. The bottom figure shows the quantum defect as a function of orbital angular momentum ℓ for $n = 100$.

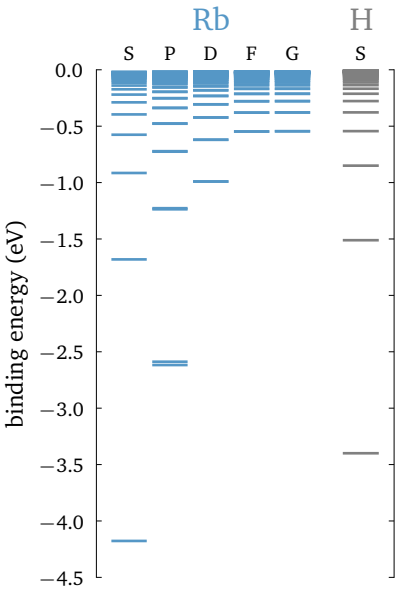

Fig. 2.2: **Energy spectrum of Rubidium and Hydrogen atoms.** Binding energy of Rubidium are depicted in blue and for Hydrogen in grey. For Rb each column represents a different azimuthal quantum number. Note that for higher azimuthal angular momentum Rb spectrum is similar to H.

Most Rydberg properties used in this thesis are calculated with the "Alkali Rydberg Calculator" by Šibalić et al., 2017 (a Python programming language package).

2.2.2 Rydberg wave functions

The Alkali Rydberg wave functions can be calculated using the non-relativistic Schrödinger equation

$$\left(-\frac{\hbar^2}{2\mu}\nabla + V(r)\right)\Psi(r,\theta,\phi) = E_{nlj}\Psi(r,\theta,\phi) \tag{2.3}$$

with reduced mass $\mu = m_a m_e/(m_a + m_e)$, alkali Rydberg radial potential $V(r)$, and $E_{n\ell j}$ the binding energy given by the Rydberg equation 2.2.

Using the ansatz $\Psi(r,\theta,\phi) = R(r)Y(\theta,\phi)$ we can separate equation 2.3 in its angular and radial components. The angular part of the equation has the spherical harmonic family of functions $Y_{l,m_l}(\theta,\phi)$ as its analytic solution. The radial equation takes the form

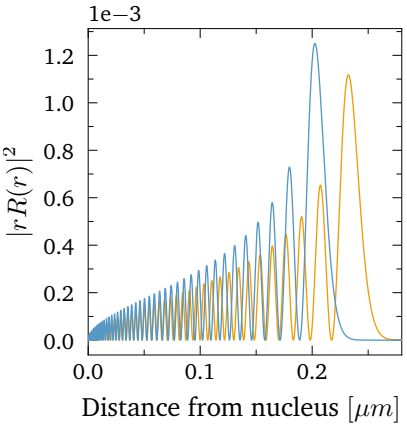

Fig. 2.3 Radial wave function. Radial wavefunction for $|48S\rangle$ state of rubidium and hydrogen.

$$\left[-\frac{1}{2\mu}\left(\frac{\mathrm{d}^2}{\mathrm{d}r^2} + \frac{2}{r}\frac{\mathrm{d}}{\mathrm{d}r}\right) + \frac{\ell(\ell+1)}{2\mu r^2} + V(r)\right] R_{nl}(r) = E_{n\ell j}R_{nl}(r) \tag{2.4}$$

with $V(r) = V_c(r) + V_{so}(r)$, where $V_c(r)$ is the Coulomb potential modified by the screening of the inner electrons, as discussed in Section 2.2.1,and $V_{so}(r)$ the relativistic spin-orbit coupling $V_{so}(r) = \alpha \mathbf{L}\cdot\mathbf{S}/(2r^3)$.

The modified alkali Coulomb potential $V_c(r)$ was described parametrically by Marinescu, Sadeghpour, and Dalgarno, 1994, and is given by

$$V_c(r) = -\frac{Z_{n\ell}(r)}{r} - \frac{\alpha_c}{2r^4}(1 - e^{-(r/r_c)^6}) \tag{2.5}$$

where $Z_{n\ell}(r) = 1 + (Z-1)e^{-a_1 r} - r(a_3 + a_4 r)e^{-a_2 r}$. The parameter α_c is the polarizability of the atomic element, r_c is a cutoff radius that

truncates the nonphysical contribution of the polarization potential near the origin. The model parameters were obtained by fitting the measured energy levels of each element.

The solution to equation 2.4 is done numerically and is often calculated using the recursive Numerov algorithm. As an example figure 2.3 shows the probability of finding the electron at a distance r from the atomic core.

2.2.3 Dipole element matrix

The dipole element matrix is a important atomic parameter which is used to calculated, for example, an excited state lifetime, interaction with external fields, and the interaction potentials between atom pairs. The Rydberg state is well defined by $\left|n', l', j', m'_j\right\rangle$, therefore the dipole moment between two Rydberg states can be defined as

$$\mathbf{d}_{ij} = e \left\langle n', l', j', m'_j \right| \mathbf{r}_q \left| n, l, j, m_j \right\rangle , \tag{2.6}$$

where $q = -1, 0, +1$ corresponds to σ_-, π and σ_+ polarization respectively. Following the treatment by King, 2008, the dipole element matrix can be separated in its angular and radial components using the Wigner-Eckhart theorem, and is expressed in therms of Wigner-$3j$ and Wigner-$6j$ and spherical basis $\mathbf{e}^q$ where the unit vectors are $\mathbf{e}^0 = \mathbf{e}^\mathbf{z}$ and $\mathbf{e}^{\pm 1} = \mp 1/\sqrt{2}(\mathbf{e}^\mathbf{x} \mp i\mathbf{e}^\mathbf{y})$. The resulting dipole element matrix is given by

$$\begin{aligned}
\mathbf{d}_{ij} &= e \left\langle i \right| \hat{\mathbf{r}} \left| j \right\rangle = e \left\langle n', l', j', m'_j \right| \hat{\mathbf{r}} \left| n, l, j, m_j \right\rangle \\
&= e\mathcal{R}_{nl}^{n'l'} \delta_{|l-l'|,1} (-1)^{j'+j+l_>+s'+1-m'_j} \sqrt{(l_>)(2j'+1)(2j+1)} \\
&\times \begin{Bmatrix} \ell & \ell' & 1 \\ j' & j & s \end{Bmatrix} \sum_q \mathbf{e}^q \begin{pmatrix} j & j' & 1 \\ m_j & -m'_j & q \end{pmatrix}
\end{aligned} \tag{2.7}$$

where $l_>$ is the bigger of l and l', $\delta_{|l-l'|,1}$ the Kronecker delta function, which gives the $|l - l'| = 1$ selection rule for optical transitions. Finally, the radial integral is calculated from the radial wave functions $\mathcal{R}_{nl}^{n'l'} = \int_0^\infty R^*_{n,\ell}(r) r R_{n',\ell'}(r) r^2 \mathrm{d}r$ and is independent of the spin-orbit coupling.

The Wigner-3j symbols define the direction of the dipole element matrix, and it implies that the dipole component in q direction is non vanishing for $|j - j'| \leq 1$ and $m'_j - m_j = q$.

As discussed above, evaluating these dipole element matrix is necessary to calculate the Rydberg-Rydberg interactions, discussed in section 2.2.5, which will lead to a mapping to interacting spin 1/2 systems in 2.3.

The dipole moment between a Rydberg and ground state is a bit more involved. For an atom with nuclear angular momentum I, the ground states will have an hyperfine structure and are expressed in terms of the total angular momentum $F = J + I$, therefore we denote the states $|n, l, j, F, m_F\rangle$. The dipole element matrix in this case is given by Löw et al., 2012 (with the translation to King, 2008 notation by Zeiher, 2017)

$$\begin{aligned}
\mathbf{d}_{ij} &= e \left\langle n', l', j', m'_j \right| \hat{\mathbf{r}} \left| n, l, j, F, m_F \right\rangle \\
&= e\mathcal{R}^{n'l'}_{nl} \delta_{|l-l'|,1} (-1)^{j+2j'-I+m_F+m'_j+S+l} \\
&\times \sqrt{(l_>)(2j'+1)(2j+1)(2F+1)} \times \begin{Bmatrix} \ell & \ell' & 1 \\ j' & j & s \end{Bmatrix} \\
&\times \sum_q \mathbf{e}^q \begin{pmatrix} j & I & F \\ m'_j + q & m_F - m'_j - q & -m_F \end{pmatrix} \\
&\times \begin{pmatrix} j' & 1 & j \\ m'_j & q & -m'_j - q \end{pmatrix}
\end{aligned} \tag{2.8}$$

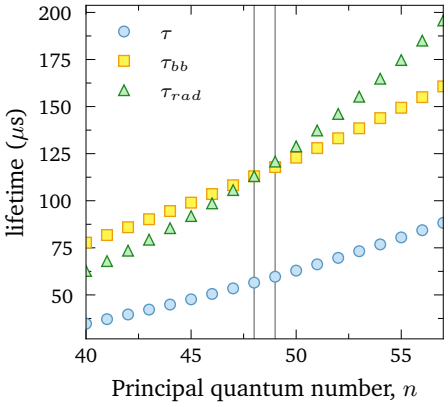

Fig. 2.4 Lifetime for Rb nS states. Lifetime of nS Rydberg states. Of particular interest is $|48S\rangle$ and $|49S\rangle$ which will be used as Rydberg spins in chapter 3 and 4. The blue circles shows the total lifetime τ, the yellow squares the lifetime due to black body radiation τ_{bb}, and the green triangles the lifetime due to spontaneous decay τ_{rad}.

2.2.4 Lifetime of Rydberg states

There lifetime τ of the Rydberg states determines the upper limit for the atomic coherence. It is composed of the radiative lifetime τ_{rad}, giving by the coupling with vacuum modes of the electromagnetic field, and the black body lifetime τ_{bb}, which accounts for the coupling with the environment thermal radiation.

$$\tau_{nl} = \left(\frac{1}{\tau^{rad}_{nl}} + \frac{1}{\tau^{bb}_{nl}} \right)^{-1} \tag{2.9}$$

According to Gallagher, 1994, the radiative lifetime can be calculated using the Einstein A coefficient with $\tau_{rad} = \left(\sum_{n'l'} A^{n',l'}_{n,l} \right)^{-1}$, where

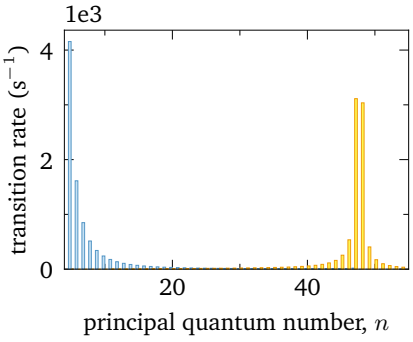

Fig. 2.5 Transition rates for Rb 48S. Transition rate from $|48S\rangle$ to $|nP\rangle$ states. The blue bars represents the spontaneous decay, and the yellow bars the coupling due to black body radiation.

$$A_{n,l}^{n',l'} = \frac{4e^2\omega_{n,l}^{n',l'}}{3\hbar c^3}\frac{l_>}{2l+1}\left(\mathcal{R}_{nl}^{n'l'}\right)^2. \tag{2.10}$$

with $\omega_{n,l}^{n',l'}$ being the energy split between the two states. And the lifetime due to the black body radiation is given by the Einstein B coefficient such that $\tau_{bb} = \left(\sum_{n'l'} B_{n,l}^{n',l'}\right)^{-1} = \left(\sum_{n'l'} A_{n,l}^{n',l'}\mathcal{N}(\omega_{n,l}^{n',l'})\right)^{-1}$ where $\mathcal{N}(\omega) = 1/\left(\exp(h\omega/k_BT) - 1\right)$ is the Bose-Einstein statistics that gives the number of photons per mode at a given temperature T. Therefore, the final expression for the black body radiation induced lifetime is

$$\tau_{bb} = \left(\sum_{n',l'} \frac{A_{n,l}^{n',l'}(\omega_{n,l}^{n',l'})}{\exp\left(h\omega_{n,l}^{n',l'}/k_BT\right) - 1}\right)^{-1}. \tag{2.11}$$

Note that $\tau_{rad} \propto n^3$ and $\tau_{bb} \propto n^2$ therefore for small n lifetime of the Rydberg state is dominated by spontaneous decays and for large n by black body radiation. Figure 2.4 shows the lifetime of $|nS\rangle$ Rydberg states, around our states of interest $|48S\rangle$ and $|49S\rangle$, which coincidentally are at the crossing between spontaneous decay and black body radiation induced decay.

One important difference between the lifetime given by spontaneous decay and by black body radiation, is that the first couples the excited state to low lying states, and the second couples it to nearby Rydberg states. Figure 2.5 shows an example for $|48S\rangle$, where the blue bars correspond to the transition rate for spontaneous decay and the yellow bars for black body induced transitions.

2.2.5 Rydberg pair interaction

In order to understand and calculate the Rydberg pairs interaction, we can write the potential as a sum of the Coulomb interactions between the electron and core (with net charge $Z = 1$ for alkali atom) of two atoms separated by a distance $\mathbf{R}_{ij}$. For a quantum description let's assume that the separation between outer electron and the core of each atom is given by the distance operators $\hat{\mathbf{r}}_i$ and $\hat{\mathbf{r}}_j$. Therefore, the sum of the Coulomb potentials is given by

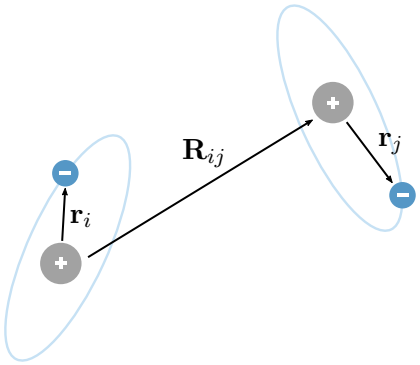

Fig. 2.6 Rydberg-Rydberg interaction. Illustration of two Rydberg atoms separated by a distance $\mathbf{R}_{ij}$, where the core of the atoms are represented as gray circles and the valence electrons as blue circles. The distance between the core and the valence electron is indicated by a distance vector $\mathbf{r}_i$ and $\mathbf{r}_j$.

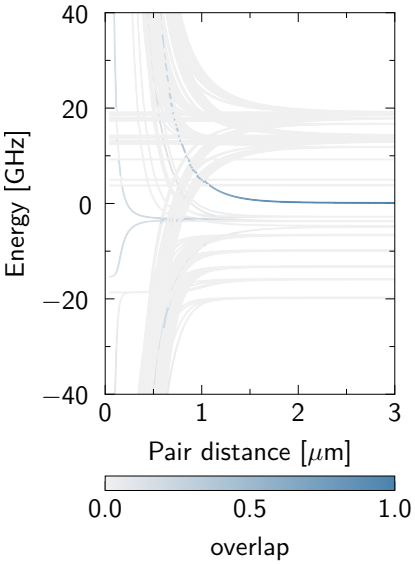

Fig. 2.7 Pair state overlap as a function of pair distance. Overlap between pair states for an initial state $|48S, 48S\rangle$. It illustrates that for $\mathbf{R}_{ij} \ll 2(\langle\hat{\mathbf{r}}_i^2\rangle^{1/2} + \langle\hat{\mathbf{r}}_j^2\rangle^{1/2})$ the interactions involve many pair states, which due to the complexity of the states energy distribution is often called the "spaghetti" region. The calculations for this figure used the Python package "Pairinteraction - A Rydberg Interaction Calculator" [Weber et al., 2017].

$$V_{ij} = \frac{e^2}{4\pi\epsilon_0}\left(\frac{1}{\mathbf{R}_{ij}} + \frac{1}{\mathbf{R}_{ij} - \hat{\mathbf{r}}_i + \hat{\mathbf{r}}_j} - \frac{1}{\mathbf{R}_{ij} - \hat{\mathbf{r}}_i} - \frac{1}{\mathbf{R}_{ij} + \hat{\mathbf{r}}_j}\right). \quad (2.12)$$

This potential can be described in a multi-pole expansion [Singer et al., 2005; Šibalić et al., 2017], if we assume that there is no overlap between the atomic wave functions. A typical criteria used to validate this assumption is that the inter-particle distance should be bigger than the LeRoy radius, meaning that $\mathbf{R}_{ij} \gg 2(\langle\hat{\mathbf{r}}_i^2\rangle^{1/2} + \langle\hat{\mathbf{r}}_j^2\rangle^{1/2})$. Keeping just the dipole-dipole term of the expansion provides us the following dipole interaction potential

$$V_{ij}^{dd} = \frac{e^2}{4\pi\epsilon_0}\left(\frac{\hat{\mathbf{r}}_i \cdot \hat{\mathbf{r}}_j}{|\mathbf{R}_{ij}|^3} - 3\frac{(\mathbf{R}_{ij} \cdot \hat{\mathbf{r}}_i)\,(\mathbf{R}_{ij} \cdot \hat{\mathbf{r}}_j)}{|\mathbf{R}_{ij}|^5}\right). \quad (2.13)$$

The element matrix of this potential can be described in terms of states $|i\rangle = |n, L, J, m_J\rangle$. Therefore,

$$\begin{aligned} V_{ij,i'j'}^{dd} &= \langle i, j|\, V_{ij}\, |i', j'\rangle \\ &= \frac{1}{4\pi\epsilon_0}\frac{\mathbf{d}_{ii'} \cdot \mathbf{d}_{jj'} - 3\,(\mathbf{d}_{ii'} \cdot \mathbf{e}_R)\,(\mathbf{d}_{jj'} \cdot \mathbf{e}_R)}{|\mathbf{R}_{ij}|^3} \end{aligned} \quad (2.14)$$

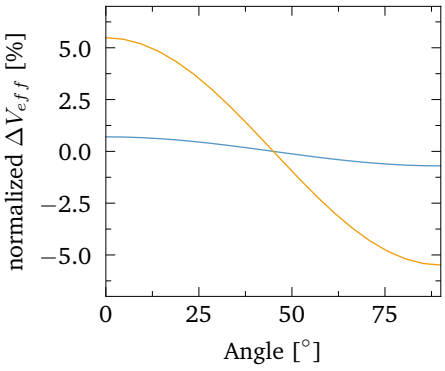

Fig. 2.8 Angular dependence of Rydberg interactions. Normalized interaction strength as a function of the angle between the atoms and their dipole (here we assume the dipoles are aligned), calculated for the van der Waals interaction between a pair of atoms in the $|48S\rangle$ state (blue line), and for a pair in $|48S\rangle$ and $|49S\rangle$ (orange line).

where $\mathbf{d}_{ij}$ is evaluated using equation 2.7, and $\mathbf{e}_R$ is the unit vector pointing at the direction of $\mathbf{R}_{ij}$.

When both dipoles are aligned in the same direction $\mathbf{d} \cdot \mathbf{e}_R = \cos(\theta)$, we have another usual representation of dipole-dipole interactions

$$V_{ij,i'j'}^{dd} = \frac{1}{4\pi\epsilon_0}\frac{|\mathbf{d}_{ii'}||\mathbf{d}_{jj'}|(1 - 3\cos^2(\theta))}{|\mathbf{R}_{ij}|^3} = \frac{C_3(\theta)}{|\mathbf{R}_{ij}|^3}. \quad (2.15)$$

Considering a two particle system with two interacting pair states, let's call it $|i, j\rangle$ and $|i', j'\rangle$, the complete Hamiltonian can be written as [Šibalić et al., 2017]

$$H_{int} = \begin{array}{c} \\ |i,j\rangle \\ |i',j'\rangle \end{array} \begin{array}{c} \begin{array}{cc} \langle i,j| & \langle i',j'| \end{array} \\ \begin{pmatrix} 0 & V^{dd} \\ V^{dd*} & \Delta_F \end{pmatrix} \end{array} \tag{2.16}$$

where $\Delta_F = E_i + E_j - E_{i'} - E_{j'}$ is called the Forster defect and it is the energy difference between the pair states. The eigen values for the pair states are

$$E_\pm = \frac{1}{2}\left(\Delta_F \pm \sqrt{{\Delta_F}^2 + 4|V^{dd}|^2}\right) \tag{2.17}$$

It is usual to separate this interaction into two regimes:

- **Resonant dipole-dipole interactions ($V^{dd} \gg \Delta_F$):** when the distance between the atoms are small, and when the Förster defect is zero, either by a choice of a resonant pair of states of by tuning it using electric fields [Ryabtsev et al., 2010], the dipole-dipole coupling dominates and the energy shift reduces to $E_\pm = \pm C_3(\theta)/|\mathbf{R}_{ij}|^3$.

- **van der Waals interactions ($V^{dd} \ll \Delta_F$):** When the Förster defect is much bigger than the interaction, which occurs for long distances in the case of a resonant pair off states, or just as a natural consequence of the choice of pair states, the interaction can be considered a second order perturbation, which leads to an energy shift of $-V^{dd}/\Delta_F = C_6/|\mathbf{R}_{ij}|^6$. Put it explicitly in terms of the pair basis, C_6 the van-der-Waals coefficient is

$$C_6 = \sum_{i',j'} \frac{\left|\langle i',j'|\, V^{dd}\, |i,j\rangle\right|^2}{\Delta_F}. \tag{2.18}$$

2.2.6 Rydberg blockade

One important result from the strong Rydberg interactions it that it can suppress simultaneous excitations of pairs of atoms if they are too close. Demonstration of this effect has being shown for individually controlled atoms [Urban et al., 2009; Gaëtan et al., 2009; Wilk et al., 2010; Isenhower et al., 2010] as well as in large ensembles [Comparat and Pillet, 2010].

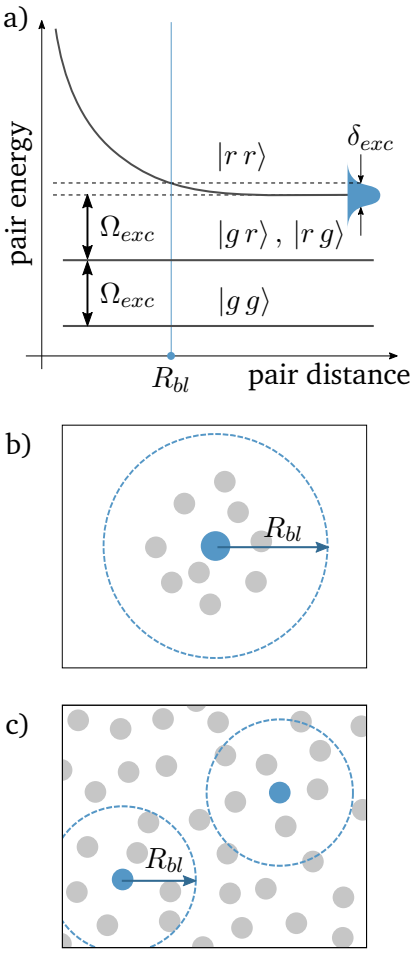

Fig. 2.9 Rydberg blockade diagram. a) for two atoms closer than the R_{bl} the ground state is coupled only to $|\psi_+\rangle$ state, not to $|rr\rangle$. **b)** illustrates the case where the R_{bl} encompasses the entire atomic ensemble. This condition is also known as super-atom picture. **c)** when the atomic ensemble is larger then the R_{bl}, the above simplifications are not possible, and the dynamics can be mapped into that of an many-body Ising spin system.

Let's consider a single atom in the ground state $|g\rangle$ coupled to a Rydberg state $|r\rangle$ by a resonant transverse field with Rabi frequency Ω and excitation bandwidth $\Delta\nu$. This atom will If The $|rr\rangle$ state is shift by $\Delta E = C_6/R^6$ due to van der Waals interactions (described in the previous section), which means that for small enough distances $R < R_{bl}$, where

$$R_{bl} = \left(\frac{|C_6|}{\hbar\Delta\nu}\right)^{1/6}, \tag{2.19}$$

it is impossible to excite both atoms to the Rydberg state (see figure 2.9 a)). It is this suppression of the double excited state that is called Rydberg blockade, and R_{bl} is the blockade radius.

In the blockade regime, the external transverse field can be described by the following Hamiltonian

$$H_{ext} = \frac{\hbar\Omega_{exc}}{2}\left(e^{i\mathbf{k}\cdot\mathbf{R_i}}\,|r\,g\rangle\,\langle g\,g| + e^{i\mathbf{k}\cdot\mathbf{R_j}}\,|g\,r\rangle\,\langle g\,g| + c.c.\right), \tag{2.20}$$

where $\mathbf{k}$ represents the excitation field wave vector, $\mathbf{R_a}$ and $\mathbf{R_b}$ corresponds to the position of atom a and b. Using the entangled states basis $|\psi_\pm\rangle = e^{i\mathbf{k}\cdot\mathbf{R_a}}\,|r\,g\rangle \pm e^{i\mathbf{k}\cdot\mathbf{R_b}}\,|g\,r\rangle$ instead of $|g\,r\rangle$ and $|r\,g\rangle$, one finds that the external field couples $|g\,g\rangle$ and $|\psi_+\rangle$ with a enhanced Rabi frequency given by $\Omega_{N=2} = \sqrt{2}\Omega_{exc}$. The state $|\psi_-\rangle$ is not excited by the field.

This reasoning can be easily extended to an ensemble of N atoms if the maximum pair distance is smaller than the blockade radius, $max\{|\vec{R}_i - \vec{R}_j|\} < R_{bl}$, as illustrated in figure 2.9 b). In such cases we can truncate the Hilbert space to a many body state where all atoms share only one Rydberg excitation $|R\rangle = \frac{1}{\sqrt{N}}\sum_{i=1}^{N}|g_1...g_{i-1}\,r_i\,g_{i+1}...g_N\rangle$ and a state with no excitation $|G\rangle = |g_1...g_N\rangle$. In this case, the entire ensemble of N atoms participate on the collective oscillations, and the Rabi frequency enhancement is given by $\Omega_N = \sqrt{N}\Omega_{exc}$. This ensemble of atoms sharing one Rydberg excitation is usually called a super-atom [Zeiher, Schauß, et al., 2015].

If the ensemble is larger than the blockade radius, it can accommodate more than one excitation (figure 2.9 c)). In this case there is no simple solution for the dynamics of the system, and the excitations positions are strongly correlated due to the Rydberg blockade. In fact, we will shown in section 2.3 that it can be mapped into a many-boy Ising spin system.

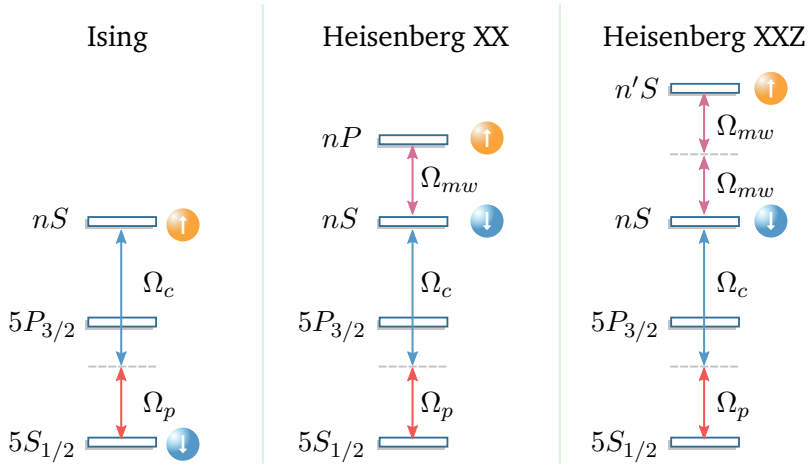

Fig. 2.10 Mapping Rydberg-Rydberg interactions to spin systems. Depending on the choice of states, different spin Hamiltonians can be achieved. Here we show three examples: Ising, by mapping a ground state to a Rydberg state; XY for a pair os state with resonant dipole-dipole interaction (e.g. $|nS\rangle$ and $|n'P\rangle$); and XXZ if we use a pair of states with van-der-Waals interactions (e.g. $|nS\rangle$ and $|n'S\rangle$).

2.3 Mapping Rydberg atoms to spin 1/2 systems

Off particular interest for this thesis work, is to understand how the Rydberg interactions can be used for quantum simulation of spin systems. A general Heisenberg spin Hamiltonian for a driven spin 1/2 system can be written as

$$H = \frac{1}{2}\sum_{i,j,\mu} J_{ij}^{\mu} S_{\mu}^{(i)} \hat{S}_{\mu}^{(j)} + \sum_{i,\mu} \mathcal{F}_{\mu}^{(i)} S_{\mu}^{(i)}, \tag{2.21}$$

where $\mu = (x, y, z)$, J_{ij}^{μ} is the spin-spin interaction in μ direction, $S_{\mu}^{(i)}$ is the spin 1/2 operator, and $\mathcal{F}_{\mu}^{(i)}$ represents an external field.

For the scope of this thesis we are interested in three particular forms of this Hamiltonian. Ising where $J_{ij}^{x} = J_{ij}^{y} = 0$, XX where $J_{ij}^{x} = J_{ij}^{y} = J_{ij}$ and $J_{ij}^{z} = 0$, and XXZ with $J_{ij}^{x} = J_{ij}^{y} = J_{ij}$ and $J_{ij}^{z} = \delta J_{ij}$.

2.3.1 Ising

The Ising Hamiltonian can be realized by mapping the ground state to spin down state $|\downarrow\rangle = |g\rangle$, and the Rydberg state to spin up state

$|\uparrow\rangle = |nS\rangle$. In this case we only have van der Waals interactions for the same Rydberg state (assuming that there are no Förster resonances), which lead to the following Hamiltonian [Schauss, 2018; Browaeys and Lahaye, 2020]

$$H_{gr} = \frac{1}{2}\sum_{i\neq j} J_{ij}\sigma_{\uparrow\uparrow}^{(i)}\sigma_{\uparrow\uparrow}^{(j)} \tag{2.22}$$

where $\sigma_{\uparrow\uparrow} = |\uparrow\rangle\langle\uparrow|$, and $J_{ij} = -C_6/{r_{ij}}^6$. This equation can be expressed in using spin 1/2 operators using the relation $\sigma_{\uparrow\uparrow}^{(i)} = \mathbb{1}/2 + S_z^{(i)}$, where $\mathbb{1}$ is the identity operator. Therefore

$$H_{gr} = \frac{1}{2}\sum_{i\neq j} J_{ij}S_z^{(i)}S_z^{(j)} + \sum_i \mathcal{F}_z^{(i)}S_z^{(i)} \tag{2.23}$$

with $\mathcal{F}_z^{(i)} = \sum_{j(j\neq i)} J_{ij}/2$. As described by Schauss, 2018, for a finite system $\mathcal{F}_z^{(i)}$ assume lower values at the edge of the system, therefore it has the effect of concentrating the Rydberg excitations in this region. Note that H_{gr} now has the driven Ising Hamiltonian form with $J_{ij}^z = C_6/{r_{ij}}^6$ and "field" in the z direction.

The excitation of Rydberg atoms from the ground state can be described by this Hamiltonian by adding a transverse field. Let's define the external field Rabi frequency as Ω_{exc} with phase ϕ_{exc} and detuning Δ_{exc}, then the Hamiltonian takes the form

$$H_{gr} = \frac{1}{2}\sum_{i\neq j} J_{ij}S_z^{(i)}S_z^{(j)} + \sum_{i,\mu} \mathcal{F}_\mu^{(i)}S_\mu^{(i)}, \tag{2.24}$$

with the Ising interaction given by $J_{ij} = C_6/{r_{ij}}^6$, and the field by $\mathcal{F}_x^{(i)} = \Omega_{exc}\cos(\phi_{exc})$, $\mathcal{F}_y^{(i)} = \Omega_{exc}\sin(\phi_{exc})$, and $\mathcal{F}_z^{(i)} = \sum_{j(j\neq i)} J_{ij}/2 - \Delta_{exc}$.

2.3.2 XY

The XY Hamiltonian is achieved by mapping two Rydberg states, with dipolar interaction, onto a spin 1/2 system. For example, let's assume $|\downarrow\rangle = |nS\rangle$ and $|\uparrow\rangle = |nP\rangle$. Then the interaction Hamiltonian is given by

$$H_{sp} = \frac{1}{2}\sum_{i\neq j} J_{ij}\left(S_x^{(i)}S_x^{(j)} + S_y^{(i)}S_y^{(j)}\right), \tag{2.25}$$

with $J_{ij} = C_3/{r_{ij}}^3\left(1-3\cos^2(\theta_{ij})\right)$ where θ_{ij} is the angle of the vector r_{ij} with the quantization axis [Franz, 2018].

2.3.3 XXZ

To obtain an XXZ spin Hamiltonian we choose two different Rydberg states that are coupled by van der Waals interaction, for example $|\downarrow\rangle = |n_1 S\rangle$ and $|\uparrow\rangle = |n_2 S\rangle$ with

$$H_{vdW} = -\frac{1}{\hbar}\sum_m \frac{H_{DDI}\,|m\rangle\,\langle m|\,H_{DDI}}{\Delta_F}\delta\left(\omega_{fm}+\omega_{mi}\right)$$

where the Förster defect $\Delta_F = E_m - E_i$ is the difference between the intermediate and the initial state, and $\delta(\omega)$ is the Dirac delta function. We can write the interaction Hamiltonian in the spin pair basis in matrix form

$$H_{i,j}^{int} = \frac{1}{|\mathbf{R}_{ij}|^6}\begin{array}{c} \\ |\downarrow\downarrow\rangle \\ |\downarrow\uparrow\rangle \\ |\uparrow\downarrow\rangle \\ |\uparrow\uparrow\rangle \end{array}\begin{array}{c} \begin{array}{cccc} \langle\downarrow\downarrow| & \langle\downarrow\uparrow| & \langle\uparrow\downarrow| & \langle\uparrow\uparrow| \end{array} \\ \begin{pmatrix} C_{6\downarrow\downarrow} & 0 & 0 & 0 \\ 0 & C_{6\downarrow\uparrow} & \widetilde{C}_{6\downarrow\uparrow} & 0 \\ 0 & \widetilde{C}_{6\uparrow\downarrow} & C_{6\uparrow\downarrow} & 0 \\ 0 & 0 & 0 & C_{6\uparrow\uparrow} \end{pmatrix} \end{array} \tag{2.26}$$

which can be identified as the Heisenberg XXZ Hamiltonian

$$H_{ij} = \frac{1}{2}\sum_{i,j} J_{i,j}\left(S_x^{(i)}S_x^{(j)} + S_y^{(i)}S_y^{(j)} + \delta S_z^{(i)}S_z^{(j)}\right) + \sum_i \Delta_{vdW} S_z^{(i)}$$

with $J_{i,j} = \widetilde{C}_{6\uparrow\downarrow}/|\mathbf{R}_{ij}|^6$, $\delta = \left(C_{6\downarrow\downarrow} + C_{6\uparrow\uparrow} - 2C_{6\downarrow\uparrow}\right)/\widetilde{C}_{6\uparrow\downarrow}$, and $\Delta_{vdW} = \left(C_{6\downarrow\downarrow} - C_{6\uparrow\uparrow}\right)/2|\mathbf{R}_{ij}|^6$. The additional spin detuning, the last term in the Hamiltonian, is an order of magnitude smaller then the interaction strength J_{ij}, and can thus be ignored.

2.4 Determination of the Rydberg spin distribution

In the previous section we noted that the excitation of Rydberg atoms from the ground state can be mapped onto an Ising spin system. As already discussed it is a hard problem to solve its dynamical evolution numerically. Nevertheless, knowing (or estimating) the initial spatial distribution of the spins is important for our experiments. From the spins pair distance distribution we can calculate the interactions, allowing for an estimation of the mean field interaction and nearest neighbor interaction for example. This information important for chapter 4 as it will be used as an input for semi-classical simulations of the spin dynamics (see section 4.3).

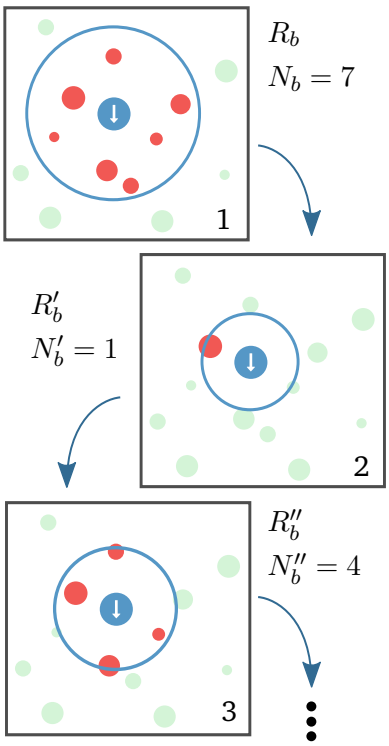

Fig. 2.11: **Illustration of the self consistent blockade method.** In this example the one Rydberg atom is excited (blue circle) from an ensemble of ground state atoms. We initialize the number of blockaded atoms to zero $N_{bl} = 0$ and calculate the Rydberg blockade R_{bl}. In a next step, we update N_{bl} and recalculate the blockade radios R_{bl} which now will be smaller than in the first step. This process is repeated until the values converge.

The simulation is based on a Monte Carlo master equation that accounts for the influence of the Rydberg blockade effect, due to which all atoms within a blockade radius follow common many-body dynamics driven by the collectively enhanced super-atom Rabi frequency.

First, we generate a randomized distribution of ground state atoms enclosed in a volume defined by the experimental geometry. Then the excitation lasers are described using Gaussian beam equations. To each atom an excitation probability ρ_i is associated, which is determined by solving the optical Bloch equations with a dephasing γ and an enhanced Rabi frequency $\sqrt{N_{bl}} \times \Omega_{eff}$, where N_{bl} is the number of blockaded atoms per super-atom. The latter is obtained self-consistently from the Rydberg blockade radius $R_{bl} = (C_6/\hbar\Delta\nu)^{1/6}$ which depends on the spectral width of the excitation $\Delta\nu$, given by the combination of the Fourier limited width, the laser linewidth and the power broadening of the enhanced Rabi frequency. Hence, the distribution of Rydberg atoms is sampled by exciting each atom with its probability ρ_i, unless they lay within the blockaded volume of an already excited atom where their excitation is suppressed.

To simulate the Rydberg atom distribution of our experiments we tune the local effective Rabi frequency in order to match the total number of Rydberg atoms obtained in the experiment. In section 3.3.1, we show that there's is good agreement between our simplified Rydberg excitation model and measurements of the Rydberg cloud using a technique based on absorption imaging.

Experimental realization of a Heisenberg XXZ Hamiltonian using Rydberg atoms

Chapter 3

Contents

This chapter is partially based on the following publications, from which parts of the text are reproduced verbatim:

Glassy Dynamics in a Disordered Heisenberg Quantum Spin System A. Signoles, T. Franz, R. Ferracini Alves, M. Gärttner, S. Whitlock, G. Zürn, M. Weidemüller. Physical Review X, Vol. 11, No. 1 (2021)

The author contributed to the experimental apparatus, data acquisition and analysis, and a algorithm to generate the initial spin distribution for the dTWA simulations.

Depletion imaging of Rydberg atoms in cold atomic gases M. Ferreira-Cao, V. Gavryusev, T. Franz, R. Ferracini Alves, A. Signoles, G. Zürn, M. Weidemüller. J. Phys. B, Vol. 53, No. 8 (2020)

The author contributed with experimental setup, data acquisition and analysis, simulation of the initial spin distribution, and on the interpretation of the results.

3.1 Introduction

In chapter 2 it was shown how interacting Rydberg atoms can be mapped into spin 1/2 systems. Investigations on these systems require careful preparation, readout and control of the Rydberg atoms. A well-established approach relies in the trapping of individual Rydberg atoms in optical lattices and tweezers [Labuhn et al., 2016; Barredo, Léséleuc, et al., 2016; Endres et al., 2016; Zeiher, Bijnen, et al., 2016] which allows to locally manipulate the spins. This approach allowed to study interesting many-body phenomena, such as "crystallization" of excitations [Schauß et al., 2015], exploring quantum quench dynamics [Bernien et al., 2017; Zeiher, J.-y. Choi, et al., 2017], and extracting the critical exponent of phase transitions [Keesling et al., 2019], in ordered arrays of Rydberg spins. These investigation focus mainly on 1D and 2D ordered geometries [Browaeys and Lahaye, 2020] with up to 256 Rydberg atoms

[Ebadi et al., 2021]. In this chapter, we introduce an approach which is a bit distinct. We excite the Rydberg atoms directly from a large dipole trap which has several consequences. On the one hand, this approach allows us to simulate many-body dynamics on the order of thousand spins in a 3D configuration, which is currently not possible with optical lattices or tweezers (that the author is aware, the maximum number of atoms assembled in 3D is 72 [Barredo, Lienhard, et al., 2018]). On the other hand, the Rydberg atoms get randomly excited, which directly translates in a disordered Rydberg spin distribution with correlation in the position given by the Rydberg blockade and enables the investigation of disordered quantum spin systems. Furthermore, instead of controlling and reading out each Rydberg spin individually, we rather manipulate them globally and readout their magnetization by a technique based on field ionization.

In this chapter we explain our experimental setup (see figure 3.1) and the different techniques used for the spin simulation. The structure of this chapter is as follows. It starts in section 3.2 with the ground state preparation, which consists of using standard atom cooling techniques to create a cold Rb sample. Then in section 3.3 the Rydberg excitation is described, were a two-photon coupling transfers atoms from $|g\rangle$ to $|\downarrow\rangle = |nS\rangle$. In this section we also describe an optical technique called depletion imaging that is used to characterize the Rydberg atom cloud. Section 3.4 presents the method used to couple two Rydberg nS-states. This allows for the first experimental implementation of Heisenberg XXZ-models using Rydberg atoms. Finally, section 3.5 explains how we can extract the magnetization of the Rydberg spin system.

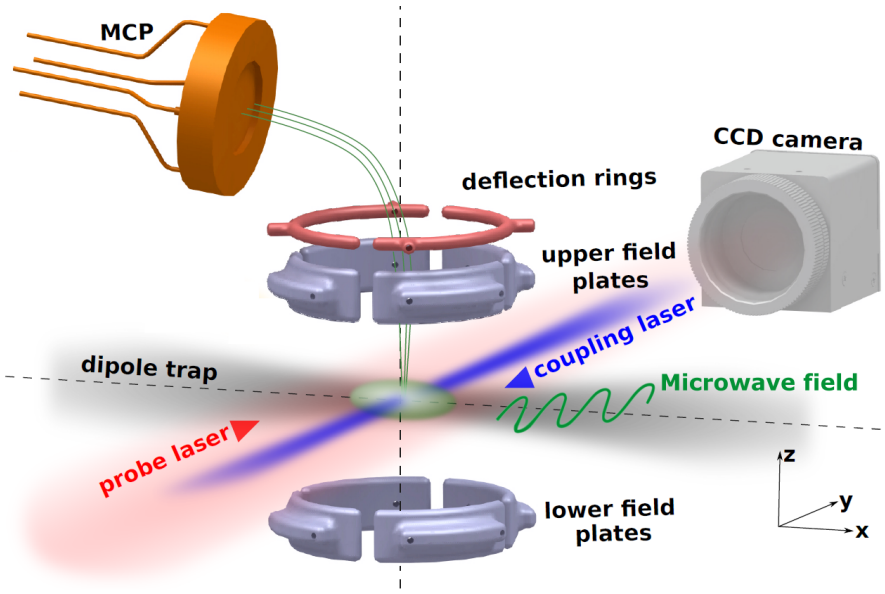

Fig. 3.1 Setup for preparation and detection of Rydberg atoms in an ultracold ^{87}Rb gas. Pre-cooled atoms are transferred from a magneto-optical trap into the reservoir optical dipole trap. An additional tight dipole trap in the vertical direction may be employed to create mesoscopic samples. After being released from the trap, the atoms are excited to Rydberg states by a combination of a 780nm laser, a counter-propagating 480nm coupling laser and microwave radiation at $2-67$GHz. An electrode structure composed of 8 field plates is used for precise electric field control and field ionization of Rydberg atoms. Two deflection rings guide the ions (green trajectories) onto a micro-channel plate (MCP) detector. Spatial information on the distribution of ground-state atoms is acquired in parallel by absorption imaging with a CCD camera. Taken from Ferreira Cao, 2017.

3.2 Ground state preparation

The ultracold atomic samples of ^{87}Rb are initially prepared using standard cooling techniques [Foot, 2005; Harold J. Metcalf, 2012]. This preparation is done in two main steps for the Rydberg spins experiment. We load a 3D magneto-optical trap (MOT), and subsequently transfer the atoms to a crossing dipole trap. For the experiments described in this thesis, the phase space density of a single crossing dipole is sufficient, therefore the cooling and trapping procedure is simpler than what is described in a previous report about our experimental setup [Hofmann et al., 2013].

Fast experimental cycle is necessary to get good data statistics in reasonable time. In our experiment, it is dominated by the 3D MOT loading time, therefore a good capturing efficiency is important. This is achieved by using a 2D MOT that provides a cold source of Rubidium atoms, with high atomic flux, small beam divergence, and relative slow velocity. These combined attributes result in typical loading rates of the order of 10^9 atoms per second [Höltkemeier, 2011; Busche, 2011]. With this rate experimental cycles of the order of one second are achieved. Another advantage of the 2D MOT source is that it does not produce ions, which can be a problem due to the extreme sensitivity of Rydberg states to stray electric fields [Comparat and Pillet, 2010].

The dipole trap used consists of two weakly focused beams, generated by a 55W Mephisto MOPA laser at 1064 nm wavelength. The two beams have a 5° angle between them and are aligned in order to have a coincident focal point. The result is a cigar shape trap with dimensions of approximately $60\mu m \times 60\mu m \times 250\mu m$ at $1/e^2$. This geometry gives a decent phase-space overlap with the MOT trap, resulting in an efficient atomic transfer, where a typical $5 \cdot 10^{11} cm^{-3}$ atom density at $40\mu K$ of temperature is achieved. The design of this trap has being modified from Hofmann et al., 2013 where previously the crossing dipole trap was implemented by imaging diffraction orders of an AOD. We now use an aligned retro-reflection, increasing the trap depth due to the extra power available on this configuration.

It is worth to note that the dipole trap beams have a 45° angle with respect to the blue beam of the two-photon excitation. This has to be accounted for when computing the Rydberg excitation volume and optical densities (see section 3.3.1)).

To avoid atom losses during the transfer to the dipole trap, the atomic states are pumped to the $|5S_{1/2}, F = 1\rangle$ manifold avoiding hyperfine changing collisions. This is done by removing the pumping beam 2 ms before the transfer.

After the dipole trap loading, all atoms are still occupying the $|F = 1\rangle$ manifold. In order to start the Rydberg excitation process from a well defined state, we transfer the atoms into the $\left|5S_{1/2}, F = 2, m_F = 2\right\rangle = |g\rangle$ state which will be referred as the ground state. This is performed by a controlled Landau-Zener transfer on the stretched states $|F = 1, m_F = 1\rangle$ and $|F = 2, m_F = 2\rangle$ (see figure 3.2).

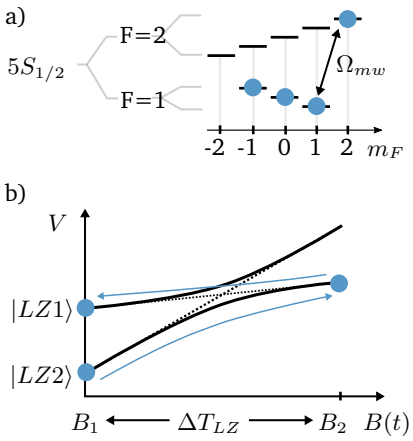

Fig. 3.2: **a) Ground states transfer scheme to $|g\rangle$.** Populated states are marked with a blue dot. Initially F=1 manifold is populated with equal distribution. Then part of atoms in the $|F = 1, m_F = 1\rangle$ are transferred to $|F = 2, m_F = 2\rangle$ using a Landau-Zener transfer. **b) Dressed states energy as a function of magnetic field $|g\rangle$.** The atoms in the dressed state $|LZ1\rangle = |F = 1, m_F = 1, N + 1\rangle$ are transferred to $|LZ2\rangle = |F = 2, m_F = 2, N\rangle$ where N accounts for the Fock state of the dressing field Ω_{mw}, by ramping the field from $B_1 = 2.7G$ to $B_2 = 3.7G$ during a time ΔT_{LZ}.

The states are coupled to microwave radiation that is resonant at a 2.9 G magnetic field. One of the internal electrodes is used as a microwave antenna for this purpose. The transfer occurs as a dynamic process. As the field strength changes at a constant rate from $B_1 = 2.7G$ to $B_2 = 3.1G$ over a time ΔT_{LZ}, the dressed states go through an avoided crossing. The adiabatic character of the transfer process is given by $v_{LZ} = \Delta B/\Delta T_{LZ}$ (see Fig 3.3). This technique allows us to control the $|g\rangle$ state density without changing the atomic cloud size and shape, but its drawback is that we can transfer just 17% of the total number of atoms. Only 1/3 are in the $|F = 1, m_F = 1\rangle$ magnetic sub-level, and the maximum efficiency of the adiabatic transfer is 51% in our setup. An improved Landau-Zener was implemented after this thesis work, where the magnetic field is kept constant and the microwave frequency is swept, offering a better degree of control. The efficiency improved to 90%. Using a simple optical pumping allows for a much higher transfer efficiency but the density control would rely on tuning a free time of flight period, which changes the sample size dimensions, and more importantly, the Rydberg excitation volume. In certain occasions we indeed allow for a period of free ballistic expansion, which can achieve orders of magnitude in ground state variation, nevertheless, this time is kept fixed throughout the experiment.

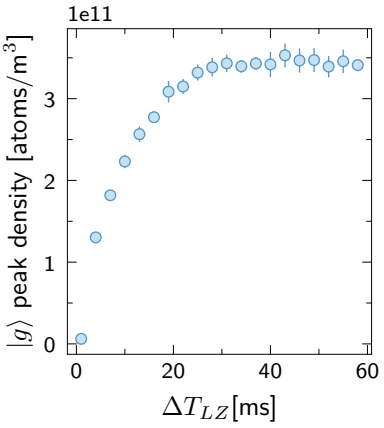

Fig. 3.3 Ground state density control. Peak density of the $|g\rangle$ state as a function of Landau-Zener transfer duration ΔT_{LZ}. The transfer hits its maximum efficiency for a duration of $\approx 30ms$.

After the dipole trap is loaded, a 6.1(1) Gauss magnetic field is applied to lift the magnetic sub-levels degeneracy, leaving the atomic system in well defined states.

3.3 Excitation of Rydberg spins from the ground state

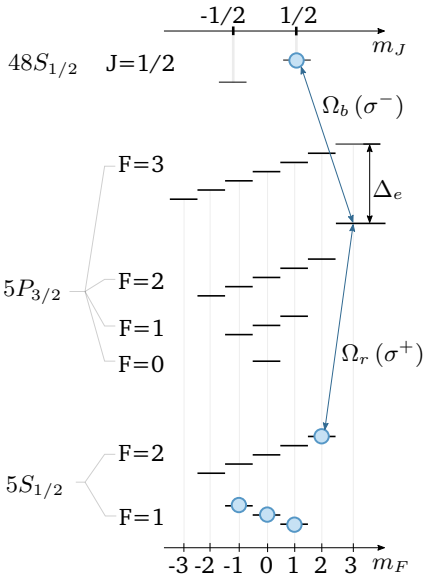

Fig. 3.4: **Rydberg excitation scheme.** This figure represents the states of interest as a black horizontal line, the vertical separation is not in proper scale. The blue circle marks the states that are populated. Blue arrows indicates the coupling of the blue and red excitation beams.

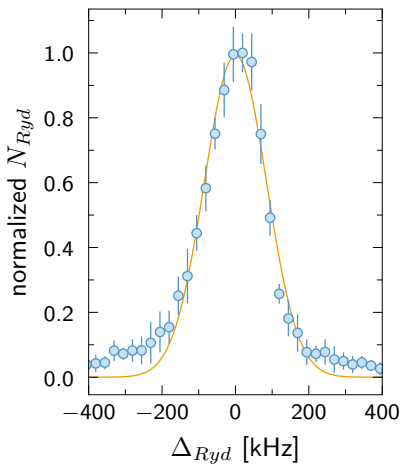

Fig. 3.5 Excitation spectrum of $|48S\rangle$. Normalized number of Rydberg atoms N_{Ry} as function 2 photon detuning Δ_{Ry}. The Doppler broadening calculated of $\approx 400\,kHz$ is relatively close to the measured linewidth. The orange line is an Gaussian fit.

After the ground state preparation, the next step in our experimental sequence is to excite Rydberg states. Figure 3.4 sketches the excitation scheme to couple the ground state $|g\rangle = |5S_{1/2}, F = 2, m_F = +2\rangle$ to the Rydberg state $|\downarrow\rangle = |48S, J = 1/2, m_J = +1/2\rangle$ via two photon resonant coupling.

Two lasers, with 780nm and 480 nm, and Rabi frequencies Ω_r and Ω_b, realize a two photon excitation from ground state $|g\rangle$ to the Rydberg state $|\downarrow\rangle$ via the intermediate excited state $|e\rangle = |5P_{3/2}, F = 3, m_F = 3\rangle$. A detuning $\Delta_e/2\pi = -97.0(4)MHz$ relative to the excited state is applied in order to avoid populating this state. Note that the separation of $|5P_{3/2}, F = 3\rangle$ and $|5P_{3/2}, F = 2\rangle$ manifolds is 267MHz, and the width of the $|5P_{3/2}, F = 3\rangle$ manifold is 34(1) MHz, so there is no single photon resonance. Nevertheless, using blue detuning as suggested by Löw et al., 2012 helps avoiding all lower lying hyperfine levels and is a more sensible choice for future experiments.

Due to the conservation of angular momentum, the excitation path requires that the red and blue lasers are set to σ^+ and σ^- polarization respectively. Nevertheless, the direction of the red beam is perpendicular to the quantization axis, restricting its it to a superposition of circular polarization σ^+ and σ^-. Special attention is needed to not couple this polarization with other states that would lead to another Rydberg excitation path. Even though we lose half probe beam power with this setup, this direction was chosen to free optical access to other components of the experiment.

Another feature of this excitation path is that the Zeeman shift of $|g\rangle$ and $|\downarrow\rangle$ are equal to $\mu_B B$, consequently the two-photon resonance of this excitation is not sensitive to changes on the magnetic field.

In the single particle regime, the Rabi frequency of the two-photon excitation is given by

$$\Omega_{Ry}^{SP} = \sqrt{\left(\frac{\Omega_r\,\Omega_b}{4\,\Delta_e}\right)^2 + {\Delta_{Ry}}^2} \tag{3.1}$$

where Δ_{Ry} is the two-photon detuning. This frequency is enhanced due to the Rydberg blockade effect by $\Omega_{Ry} = \sqrt{N_{bl}}\Omega_{Ry}$, where N_{bl} is the number of blockaded atoms in the $|g\rangle$ state. In our experiment the two-photon Rabi frequency is $\Omega_{Ry}/2\pi \approx 150\,kHz$.

Another important aspect is the excitation bandwidth δ_{exc}. As it was shown in chapter 2, it provides the scale of Rydberg blockade effect. There are a few points to consider. First, the natural linewidth of $48S_{1/2}$ state is 8.8 kHz considering natural decay and black body radiation redistribution. Power broadening takes it to 91 kHz. Ground-state atoms are at $\approx 50\,\mu K$ before excitation which gives a Doppler broadening of $\approx 400\,kHz$ for ^{87}Rb. Finally, the excitation is produced with short pulses with duration t_{exc}. These pulses vary from $0.6\,\mu s$ to $1\,\mu s$. It is short enough for the Fourier width to dominate the excitation spectrum. The Fourier width is $1\,MHz$ to $1.7\,MHz$. In total δ_{exc} ranges approximately from $1.4\,MHz$ to $2.1\,MHz$. The blockade radius R_{bl} for this range of excitation bandwidth is presented in figure 3.6.

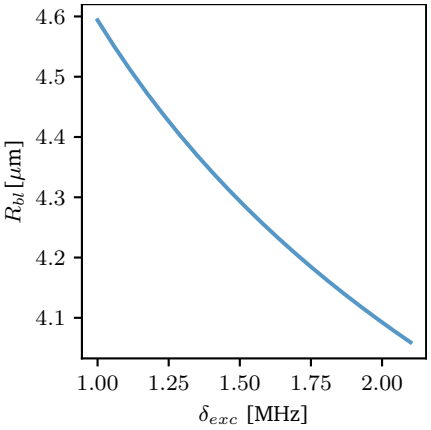

Fig. 3.6 Blockade radius. Blocked radius R_{bl} as a function of excitation bandwidth δ_{exc}. In our experiments $1.4MHz < \delta_{exc} < 2.1$ which leads to $4.0\mu m < R_{bl} < 4.6\mu m$.

3.3.1 Spatial characterization of Rydberg spins distribution*

* Taken and adapted from Ferreira Cao et al., 2020

This section describes a method to determine the integrated 2D density profile of the Rydberg distribution. The main idea is to use a standard absorption imaging technique, comparing the results of the imaging with and without the pre-excited Rydberg atoms. Ground-state atoms excited to Rydberg state will not participate in the absorption imaging process, leading to lower optical density (OD). The OD difference can be attributed to Rydberg states.

The absorption imaging uses a σ^+-polarized probe laser resonant to $|g\rangle = |5S_{1/2}, F = 2, m_F = +2\rangle \leftrightarrow |e\rangle = |5P_{3/2}, F = 3, m_F = +3\rangle$. This collimated probe beam has a Gaussian profile with a waist of 1.5 mm (at $1/e2$), and is much larger than the typical cloud size, such that we can approximate the Rabi frequency to a constant $\Omega_p/2\pi = 1.57(3)MHz$. The transmitted intensity $I(x, y)$ is captured by a CCD with single-pixel area $a_{px} = 4.28\,\mu m^2$ at the object plane. The ratio between the intensity with I_g and without atoms I_{ref} can be used to obtain the integrated 2D density of ground-state atoms

$$n_g^{2D}(x, y) = -\sigma_0^{-1}(1 + s_0)\ln[I_g/I_{ref}]. \tag{3.2}$$

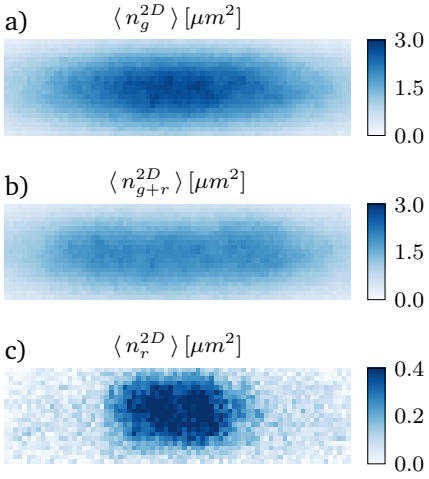

Fig. 3.7 Rydberg depletion imaging example. Typical two-dimensional density distributions observed during depletion imaging experiments, averaged over 50 realizations and with 4x4 pixel binning. (a) Groundstate density without atoms excited to the Rydberg state (peak OD = 0.7). (b) Ground state density depleted by atoms pre-excited to the Rydberg state for $t_{exc} = 3\mu s$. (c) Rydberg density obtained by depletion imaging method according to 3.3 using the absorption data presented in (a) and (b). Taken and adapted from Ferreira Cao et al., 2020.

where $n^{2D}(x,y) = \int n(x,y,z)dz$, σ_0 is the absorption cross section of the transition and $s_0 = 2\Omega_p^2/\Gamma_e^2$. For our experiments s_0 is approximately 0.13, and the resonant σ_0 for the cyclic transition we are addressing is $2.906 \times 10^{-9}\, cm^2$ (Steck, 2021).

After Rydberg excitation, part of the ground state atoms is removed. An absorption imaging under these circumstances will only measure the remaining ground state atom density n_{g+r}^{2D}. Therefore, the Rydberg density is just the difference between these two profiles $n_r^{2D} = n_g^{2D} - n_{g+r}^{2D}$. It is possible to factor out I_{ref} from the equation, leading to the following expression

$$n_r^{2D}(x,y) = -\sigma_0^{-1}(1+s_0)\ln[I_g/I_{g+r}]. \tag{3.3}$$

With this technique, it is easy to get access to the local excitation fraction, which is given by (see figure 3.7):

$$\rho_r^{2D}(x,y) = n_r^{2D}(x,y)/n_g^{2D}(x,y). \tag{3.4}$$

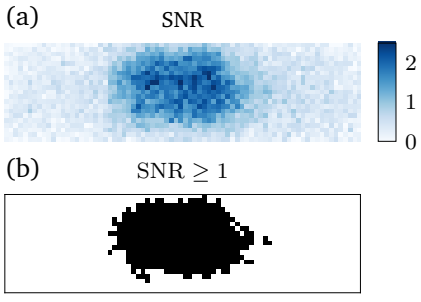

Fig. 3.8 Rydberg depletion imaging SNR. (a) SNR for depletion image of figure 3.7. (b) The binned pixels with SNR ≥ 1 are marked as black.

Our target state $|48S_{1/2}\rangle$ has a lifetime of $56.4\,\mu s$, accounting for spontaneous emission and black body radiation coupling to other states at 300 K. Since black body radiation mainly couples to nearby Rydberg states, which are not part of the absorption imaging process, the coupling to low lying P states corresponds to a higher time constant of $140.2\,\mu s$. To

be conservative, we limit the exposure time to $5\,\mu s$. Within this period, a single Rubidium atom absorbs around 10 photons, which is lower than noise in the imaging system. Therefore, to improve SNR, we make an average of 50 images, and we also bin the pixels 4 x 4 as post-processing. Considering a constant signal over the binning area, we would expect an increase in SNR by a factor of 17 compared with one frame and a single pixel. With this enhancement, we achieve SNR above 1 for most of the Rydberg cloud. Approximately 15 Rydberg atoms are needed to achieve SNR of 1 (Fig. 3.8). A possible enhancement to the sensitivity of this technique would be increasing the probe Rabi frequency and the exposure time.

This technique allow also to accomplish a spatial mapping of the excitation dynamics. By performing measurements for increasing excitation times ranging from $t_{exc} = 0.1\,\mu s$ up to $3\,\mu s$, we obtain spatially resolved maps of their two-dimensional distribution and track its time evolution. The sum of the duration of the excitation and imaging pulses is much shorter than the Rydberg state lifetime for ($\tau_{48S} = 56\,\mu s$), so the decay towards the ground state and the redistribution to neighboring states can be disregarded. Since the off-resonant 780nm excitation is active during a short time, additional dissipation due to heating of the atomic cloud during t_{exc} can also be neglected.

The experimentally observed Rydberg fraction distribution $\rho_r^{2D}(x, y)$ is shown in figure 3.9 at different excitation times, where each image bin reveals the dynamics for the local Rabi frequency $\Omega_{eff}(x, y)$. Further insight into the excitation dynamics can be obtained by exploring the local temporal evolution in different areas of the sample, as depicted in Figure 3(b), where several regimes are represented: whereas the Rydberg population rapidly increases in the center of the cloud (blue), reaching saturation at $\rho_r^{2D}(x, y) \approx 0.28$, slower and linear dynamics takes place in the tails of the excitation volume (turquoise points); intermediate regimes with progressively slower evolution towards saturation can also be observed in the slopes of the Rydberg profile (green and red points). We interpret the development of local saturation (significantly below $\rho_r^{2D}(x, y) = 0.5$, expected for Rabi oscillating dynamics in non-interacting systems) as a direct consequence of the Rydberg blockade effect [Robicheaux and Hernández, 2005; Stanojevic and Côté, 2009], as described in 2.4. Thus, we can infer from the measured Rydberg fraction that an average number of 3.6 atoms is blockaded by each Rydberg excitation. In contrast to the local dynamics, the measured global number of Rydberg atoms $\langle N_r \rangle$ does not show saturation at long

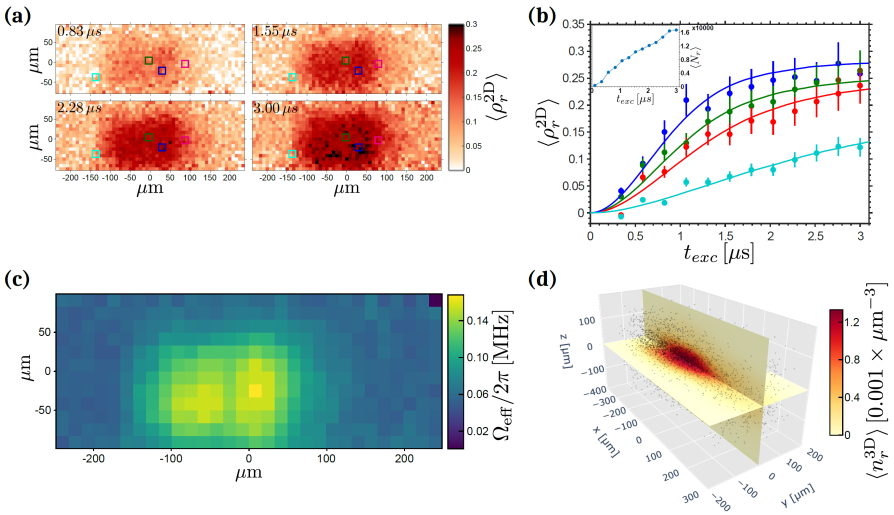

Fig. 3.9 Spatially resolved Rydberg excitation dynamics, averaged over 50 repetitions with 16 a_{px} binning. (a) Two-dimensional Rydberg fraction distribution $\rho_r^{2D}(x, y)$, integrated over **z**, for increasing excitation times of 0.83, 1.55, 2.28 and 3.00 μs. (b) Local excitation dynamics at different cloud positions, marked with hollow squares on the $\rho_r^{2D}(x, y)$ distribution in (a). The solid lines represent the simulated dynamics with the master equation Monte Carlo model, using a dephasing of $\gamma/2\pi = 0.25\,MHz$ and effective Rabi frequencies $\Omega_{eff}/2\pi = 0.17\,MHz$ (blue line), $0.14\,MHz$ (green line), $0.12\,MHz$ (red line) and $0.07\,MHz$ (turquoise line). Inset: evolution of the global mean Rydberg atom number with t_{exc}. (c) Effective Rabi frequency distribution $\Omega_{eff}(x, y)$, obtained by locally fitting the excitation dynamics with the Monte Carlo model within each 64 a_{px} bin. (d) Reconstructed 3D distribution of the Rydberg atom cloud by the Monte Carlo simulations (described in section 2.4). The dots represent a discrete Rydberg atom arrangement obtained in a single run, whereas the continuous distribution corresponds to the Rydberg density averaged over 50 realizations. Taken from Ferreira Cao et al., 2020.

excitation times t_{exc} (inset of figure 3.9 (b)). This can be attributed to the ongoing Rydberg excitation of a significant number of atoms in the tails of the distribution, where the evolution is slower and linear as full blockade has not been reached.

3.4 Rydberg spins manipulation

Since Heisenberg XXZ Hamiltonian are realized by two distinct Rydberg $|nS\rangle$ states, we need to couple $|48S, m_J = 1/2\rangle \equiv |\downarrow\rangle$ to another $|nS\rangle$ state, which we have chosen to be $|49S, m_J = 1/2\rangle \equiv |\uparrow\rangle$. The energy difference between the two $|nS\rangle$ states is 70.4 GHz, which allows us to use a microwave field to couple the them. It is a two photons process, each having a frequency of $\nu = 35.2GHz$ and goes through a detuned intermediate P-state as depicted in figure 3.10 by $\Delta_{SP} = 170MHz$. The magnetic field of 6.1G split the Zeeman sub-levels of $|nS\rangle$, $\left|nP_{1/2}\right\rangle$, and

$\left|nP_{3/2}\right\rangle$ by 17.1, 5.7 and 11.4 MHz, respectively. The we typically use a two photon Rabi frequency $\Omega_{mw}/2\pi$ is between 3 and 5 MHz (see example of figure 3.12), calibrated from the Rabi oscillations between the two spin states. The states are coupled by isochromatic photons, with no well defined polarization, therefore the two photon coupling can be achieved through different intermediate $\left|nP_{3/2}\right\rangle$ Zeeman sub-levels. Unfortunately, there will be also allowed paths coupling the spins to unwanted $|nS, m_J = -1/2\rangle$ states (see figure 3.10 red and green paths), nevertheless due to the frequency detuning of 17.1 MHz, which is large compared to Ω_{eff}, the excitation probability to these states is small ($< 3\%$).

The external field can be described in the following Hamiltonian

$$\hat{H}_{ext} = \sum_{i}^{N_s} \left[\Omega_{mw}\left(\sin\phi_{mw}\hat{S}_x^{(i)} + \cos\phi\hat{S}_y^{(i)}\right) + \Delta_{mw}\hat{S}_z^{(i)}\right] \tag{3.5}$$

where Δ is the two-photon detuning, ϕ_{mw} is the phase between the defined x axis on the Bloch sphere and N_s is the total number of spins. Note that the phase ϕ_{mw} is relative to an arbitrary definition of the coordinate system, therefore it can always be set to zero if there is only one pulse in the experimental sequence. The dynamics of $\hat{H}_{ext}$ can be visualized on the Bloch sphere (figure 3.11), which shows an arbitrary

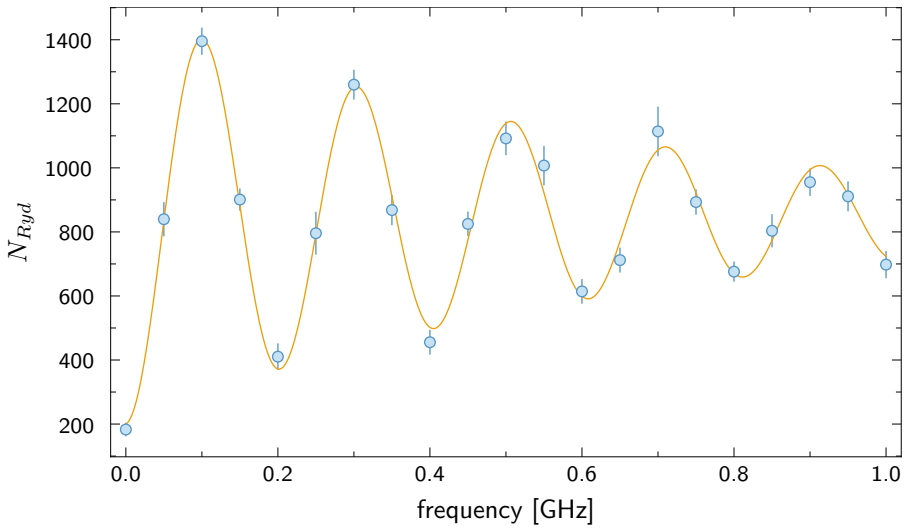

Fig. 3.12 Example of two photon Rabi oscillations between $|48S\rangle$ and $|49S\rangle$, with Rabi frequency of 4.9i(2) MHz and decay constant of 0.65(6) obtained by fitting the dumped oscillations (orange line). The short decay constant is due to Rydberg spins interaction.

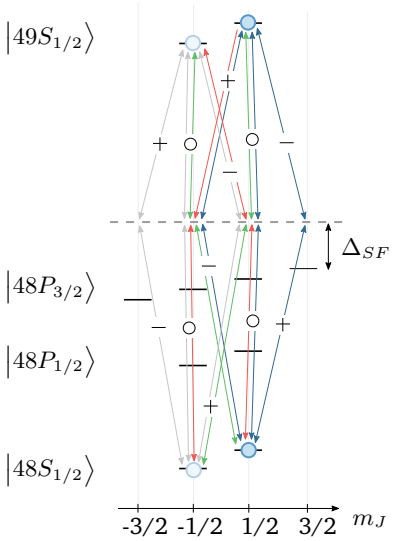

Fig. 3.10: **Microwave spin coupling**. Two photon coupling between states $|48S, m_J = +1/2\rangle$ and $|49S, m_J = +1/2\rangle$. The arrows are indicating microwave photons with σ^+, σ^-, and σ^0 polarization, indicated by the plus sign, minus sign, and circle respectively. The blue arrows shows the intended coupling paths, and the red and green arrows off resonant coupling to $|48S, m_J = -1/2\rangle$ and $|49S, m_J = -1/2\rangle$ states.

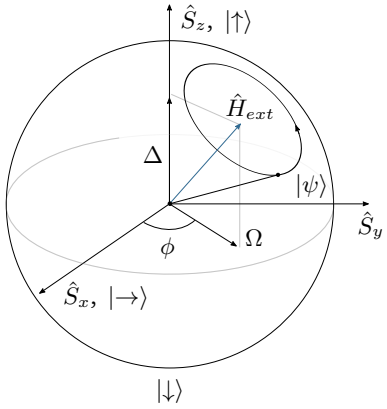

Fig. 3.11: **Spin manipulation**. Representation of a single isolated Rydberg spin state $|\psi\rangle$ in a Bloch sphere. The external field Hamiltonian $\hat{H}_{ext}$, defined in equation 3.5, rotates $|\psi\rangle$ along $\hat{H}_{ext}$ direction with angular velocity $\Omega_{eff} = \sqrt{\Omega^2 + \Delta^2}$. Here we define $|\rightarrow\rangle = 1/\sqrt{2}\,(|\downarrow\rangle + |\uparrow\rangle)$.

state $|\psi\rangle$ rotating around $\hat{H}_{ext}$ with direction defined by the Ω_{mw}, ϕ_{mw}, and Δ_{mw}. The module of the angular velocity is $\sqrt{{\Omega_{mw}}^2 + {\Delta_{mw}}^2}$.

Note that equation 3.5 assume that the rotations caused by the external microwave field are global, which means Ω_{mw}, ϕ_{mw} and Δ_{mw} is the same for all Rydberg spins. This assumption is justified since the microwave wavelength of $\approx 8\,mm$ much larger than the atoms cloud $\approx 60\,\mu m$.

The field Ω is produced by a custom microwave synthesizer, consisting in a commercial high frequency generator, mixed with phased-locked direct digital synthesizers (DDS), and an schematic description is shown in figure 3.13. A up-converter technique is used to produce phase controlled side-bands. We use a IQ mixer to favor only one side-band, thus reducing the risk of accidentally coupling the -1 side-band to another transition (see figure 3.14). Two different DDS with relative phase difference $\phi/2$ are switched in order to produce a ϕ phase difference on the two-photon coupling. In order to verify that the phase shift works, we perform a test measurement shown in figure 3.15, where we invert Rabi oscillations with a π phase shift at a certain instance of time. A quantum composer commands microwave switches to achieve nano-second pulse control which is sufficient for our experiments because our microwave and laser pulses are at micro-second scale. After the mixing stage, the final field is transmitted to the atoms by a microwave antenna which is placed in front of the view port.

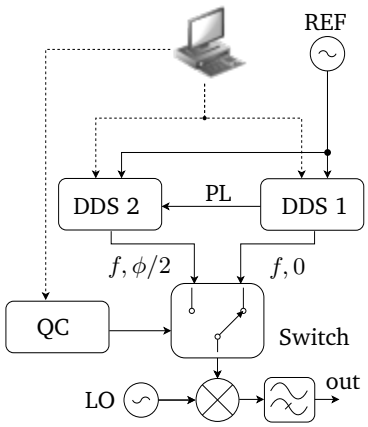

Fig. 3.13: **Microwave synthesizer setup**. Two direct digital synthesizer (DDS) working at 400MHz are phase lock and a relative ϕ is added. The signal is up-converted to $\approx$ 35 GHz by mixing it with a Anritsu MG3697C microwave synthesizer (LO). A fast switch is controlled by a quantum composer with nano-second precision.

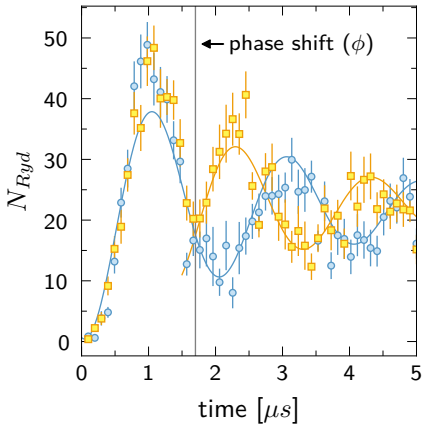

Fig. 3.15 Microwave phase shift demonstration using Rabi oscillations. This figure shows two Rabi oscillations. The blue circle (●) represents a Rabi oscillation with constant phase, and the yellow square (■) the measurement of a Rabi oscillation with the same parameters but with a phase shift at 1.7 μs. The solid lines shows a fit of a damped oscillation model where a phase shift of 0.77π.

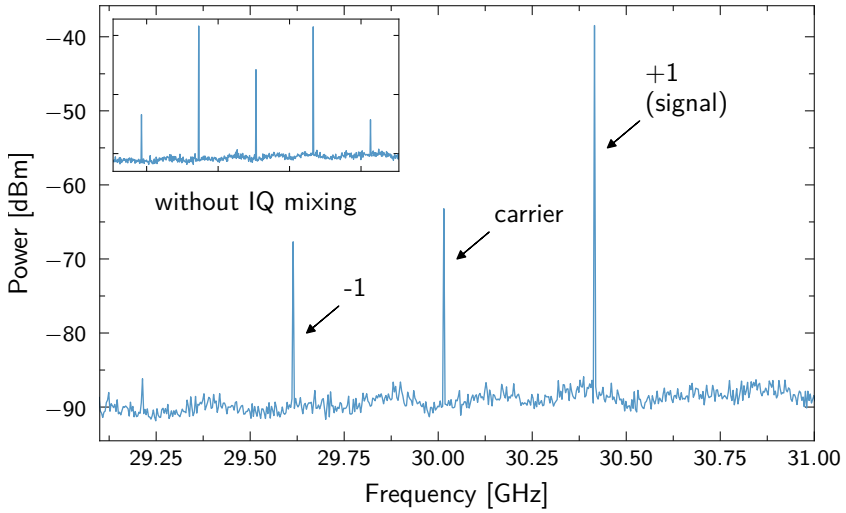

Fig. 3.14 Microwave spectrum of the signal used to manipulate the Rydberg spins. Note that due to the IQ mixer scheme, the -1 order is attenuated. The inset plot shows the signal without the IQ mixer for comparison.

Due to the large single photon detuning Δ_{SP} the single photon Rabi frequency is on the order of $55\,MHz$, one order of magnitude stronger then Ω_{mw}. In order to verify that there is no significant coupling of the microwave field with other Rydberg states, we calculate the excitation probability amplitude for pair of states close to the single photon coupling. For this calculation , the carrier and -1 side-band were also included. We only find a excitation probability amplitude of ≈ 0.02 for $\left|49S_{1/2}\right\rangle \leftrightarrow \left|48P_{3/2}\right\rangle$ and $\left|48S_{1/2}\right\rangle \leftrightarrow \left|48P_{3/2}\right\rangle$, mainly due to single photon coupling with $+1$ side-band (see figure 3.16). Therefore, we are ruling out any significant coupling to other states.

Another important aspect of the microwave system is its temporal stability. We rely on statistical averages of many repetitions of our experiments in order to improve the SNR of the extracted observables. Therefore it is important that Ω_{mw} is stable during consecutive runs of the experiment. Even though, the microwave synthesizer has a very stable power output, we inferred that there is a noticeable power fluctuation on the Rydberg atoms, since we observe it in the signal recorded by a second antenna after the experimental chamber. We believe this can be attributed to an intensity pattern emerging from interference between multiple reflections of the microwave field in the experimental setup. However, the dephasing due to the microwave power variation is on the order of 10 μs [Ferreira Cao, 2017], and since the simulations reported in this thesis are based on $\pi/2$ pulses with width of less than 1 μs, we can disregard the of the impact of the amplitude variation on our experiments.

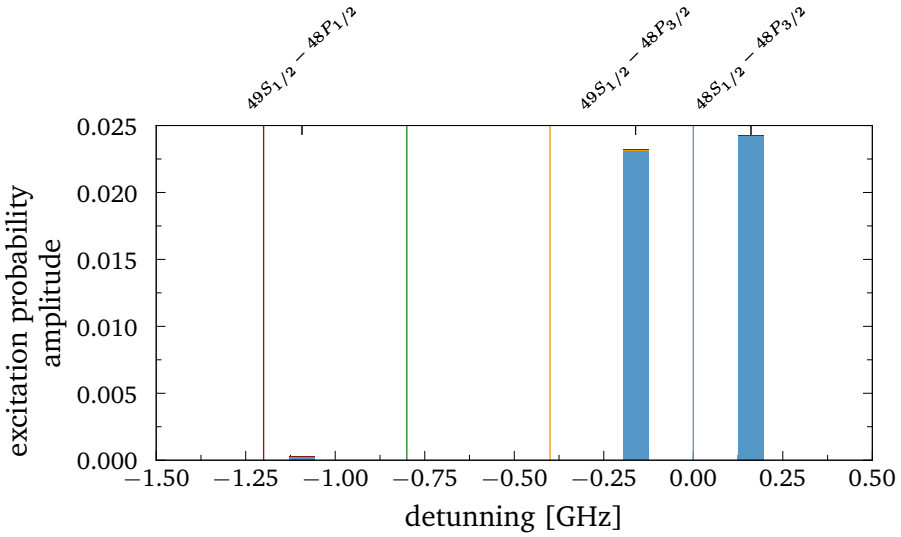

Fig. 3.16 Excitation probability for a single photon coupling of the microwave field with nearby states. The states are placed with respect to the energy detuning from the +1 side-band, and on the upper part of the plot there is a label indicating which transition is being excited. The vertical solid lines are marking the microwave peak location -2, -1, 0, +1 corresponding to blue, yellow, green, and red colors respectively. The excitation probability shown in the plot is dominated by the +1 side-band.

3.5 Construction of the magnetization

After having prepared the Rydberg sample and performed spin manipulation with the microwave field, it is important to readout meaningful observables in the system. We chosen the magnetization as our main observable, because it can be considered one important parameter in many-body spin systems and is also suitable for our experimental setup because it is a non-local property. In our system the its construction involves several steps which combines the detection of Rydberg atoms through field ionization and optical de-excitation of the down state in order to distinguish the two Rydberg states. To map out all three magnetization components in x and y direction, we apply a tomographic readout pulse before the ionization. The goal of this section is to go through the different steps needed to construct the magnetization.

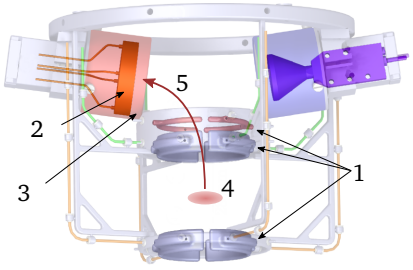

Fig. 3.17: **Electrodes and ions trajectory**. Representation of the electrodes structure and MCP detector inside the vacuum chamber. 1) indicates the electrodes, 2) the MCP detector, 3) the Faraday cage around the detector, 4) the atomic cloud, and 5) represents the Rydberg ions trajectories towards the MCP detector guided by the surround electrodes voltages. Taken and adapted from Günter, 2014.

3.5.1 Field ionization and ion detection

In order to detect Rydberg states, standard absorption and fluorescence techniques are not suitable since their scattering rate is orders of magnitude lower than for ground states. The most common method is to

ionize the Rydberg states by applying an electric field and direct the ions towards a micro-channel plate (MCP) detector [Gallagher, 1994].

By applying an electric field $E\hat{z}$ the valence electron potential is given by the Coulomb potential from the core and the additional external field $V = -1/r + E\,z$. The external field creates a saddle point at $z_{saddle} = \sqrt{E}$ with an energy given by $V(z_{saddle}) = -2\sqrt{E}$. For $48S_{1/2}$ binding energy is -54.5 cm^{-1} and the classical threshold is 79.3 V/cm. This gives just the order of magnitude for the required ionization field, because the field projects the initial state into different Stark states, each having its own classical ionization limit and tunnelling rate, making an accurate calculation for the ionization rates a complex computational task.

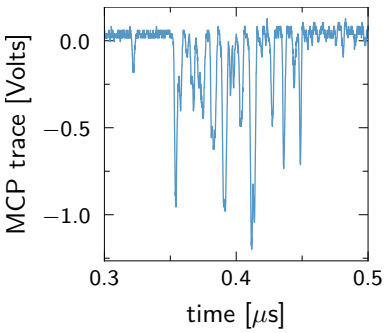

Fig. 3.18 Typical MCP ion signal. This curve shows a typical time-resolved MCP signal produced by ionizing the Rydberg spins ensemble. The number of Rydberg atoms is assumed to be proportional to the area of the MCP trace.

As it is shown in figure 3.17, inside the vacuum chamber and around the cold atom trap, eight electrodes are used to create the ionization electric field. Two additional electrodes above are used to bend the Rydberg ions trajectory towards the MCP detector. Bipolar high voltage switches (Behlke) are used to dynamically control the fields with a limiting raise time of approximately 300 ns. A faraday cage around the MCP impedes that the high voltage of the detector to affect the atoms on the trapping region. The geometry of these electrodes was extensively optimized by numerical simulations [Müller, 2010], which lead to it's present configuration.

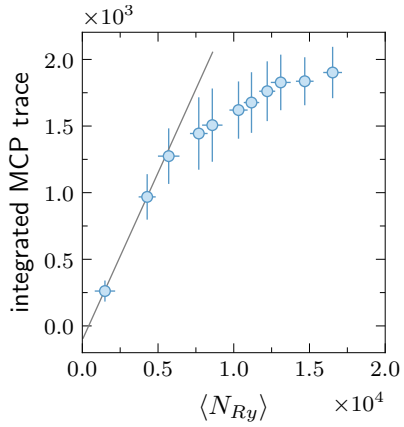

Fig. 3.19 MCP signal calibration. The integrated MCP signal (from 3.18) is shown as a function of the average Rydberg density measured by the depletion imaging technique. For the linear regime (before saturation) a detection efficiency of $\eta = 0.173 \pm 0.043$ is calculated.

The MCP signal, generated by the ionized Rydberg atoms, is recorded by a fast oscilloscope with 0.1 ns of resolution. Figure 3.18 shows a typical ion trace signal for the experiments realized during this thesis. The signal from the Rydberg ions hitting the detector is extracted by integrating it bellow a threshold. Figure 3.19 shows a calibration of the MCP signal using the depletion imaging technique of section 3.3.1. The curve shows saturation for high number of Rydberg atoms, but for the Rydberg spins simulations described in thesis (chapter 4), we work only in the linear regime.

Finally, we also take advantage of the field ionization electrodes inside the vacuum chamber, shown in figure 3.17, for compensating stray electric fields, and as an antenna for the Landau-Zener ground state excitation, described in section 3.2.

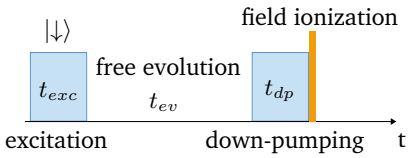

Fig. 3.20: **Optical de-excitation experiment sequence**. Fist the atoms are excited to the $|\downarrow\rangle$ state as descibed in section 3.3 during excitation time t_{exc}. Then the Rydberg states go though a period of free evolution t_{ev}. Next, a laser resonant to $|\downarrow\rangle$ and $|5P_{3/2}, F = 3, m_F = +3\rangle$ is applyed during t_{dp} depleting the $|\downarrow\rangle$ population. Finally, the Rydberg states are ionized and the ions are counted.

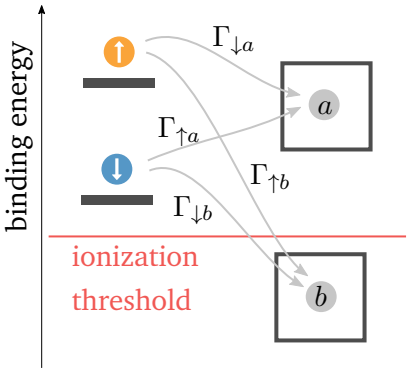

Fig. 3.21: **Four level approximation**. Representation of the four level approximation scheme where the spin states have a decay rate to shelfing states. As discussed in chapter 2, Rydberg states can decay to ground states but also to nearby states due to black body radation. These nearby states can be devided in detectable and undetectable by the field ionization techninque.

3.5.2 Optical de-excitation of the spin down state

As discussed in the previous section, the field ionization method for Rydberg detection is not state selective, but in order to observe the spin dynamics it is necessary to measure a single spin component after the read-out microwave pulse. To overcome this limitation, we apply a laser pulse resonant to $|\downarrow\rangle$ and $|5P_{3/2}, m_F = +3\rangle$ states, removing atom in $|\downarrow\rangle$ state before field ionization. The excited state $|5P_{3/2}, m_F = +3\rangle$ has a decay rate $\Gamma_e/2\pi = 6MHz$ to the ground state, and if a long enough pulse is applied, in principle, the population of $|\downarrow\rangle$ state can be completely depleted. Figure 3.20 shows a simplified experimental sequence used to characterize the optical de-excitation technique, and a typical measurement is presented in Figure 3.22 where the inset shows representation of the level scheme.

Section 2.2.4 discussed the theory of Rydberg lifetime and showed that Rydberg states are coupled to other nearby states by black-body radiation. Therefore, after optical de-excitation $|\downarrow\rangle$ the field ionization will not only count the atoms in $|\uparrow\rangle$ state, but also the fraction of atoms that transitioned to other Rydberg states which are above the ionization threshold. This system can be described using an effective four state system comprised of the spin states and two shelving states $|a\rangle$ and $|b\rangle$ representing all states above and below the field ionization threshold. For the de-excitation measurements only $|\downarrow\rangle$ is excited though.

3.5.3 Calculating the magnetization

Simply applying the above mentioned scheme which combines optical de-excitation and field ionization allows us to reconstruct the z-magnetization of the system. In order to map out the magnetization in the xy-plane we apply another $\pi/2$ readout pulse with a adjustable phase ϕ. This transfers the magnetization components from the xy-plane into our measurement basis, a technique known from tomography. We measure the magnetization $\langle S(\phi)\rangle$ by counting the $|\uparrow\rangle$ population $N_\uparrow(\phi)$ and the total number of spins $N_{\uparrow+\downarrow}$ after a $\pi/2$ readout pulse with phase ϕ.

$$\langle S_\phi\rangle = \frac{N_\uparrow(\phi) - N_\downarrow(\phi)}{2N_{\downarrow+\uparrow}} = \frac{N_\uparrow(\phi)}{N_{\downarrow+\uparrow}} - \frac{1}{2}. \tag{3.6}$$

Also from last section, it was discussed that the optical de-excitation technique measure all the states above the ionization threshold, therefore the measurements $M_\uparrow(\phi)$ and $M_{\downarrow+\uparrow}$ also include Rydberg states above

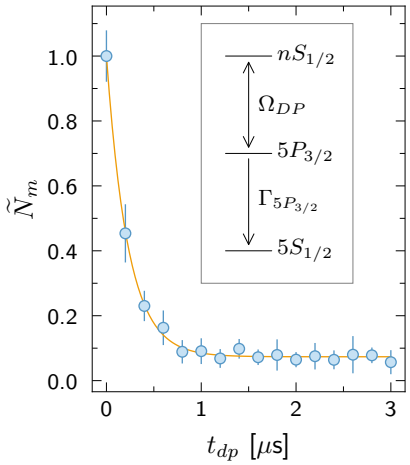

Fig. 3.22 Normalized number of Rydberg atoms measured using field ionization, after a optical de-excitation pulse with duration t_{dp}. There is no time interval between Rydberg excitation and the optical de-excitation pulse ($t_{ev} = 0$). The orange line shows an exponential decay fit with decay constant of $4.38(3)MHz$. The inset shows a representation of the optical de-excitation scheme. For the experiments presented in this thesis $T_{dp} = 1.5\mu s$ is used to guarantee maximum depletion. The measured optical de-excitation efficiency is $93(3)\%$.

the ionization threshold which were populated by black body radiation.

$$M_{\uparrow}(\phi) = N_{\uparrow}(\phi) + N_a, \tag{3.7}$$

$$M_{\downarrow+\uparrow} = N_{\downarrow+\uparrow} + N_a. \tag{3.8}$$

The total spin population $M_{\uparrow+\downarrow}$ is calibrated by field ionizing the Rydberg states after the Rydberg excitation. The $M_{\uparrow}(\phi)$ measurement is achieved by depleting the $|\downarrow\rangle$ states with the optical de-excitation technique described on the last section, and afterwards applying field ionization and counting the ions generated.

To measure the magnetization in the xy plane, the phaseϕ of the readout pulse is scanned between 0 and 2π leading to a measurement set similar to what is shown in figure 3.23. The magnetization dependency to the readout pulse phase ϕ is a sinusoidal function

$$M_{\uparrow}(\phi) = \frac{A}{2}\sin(\phi + \phi_S) + \overline{M}_{\uparrow}, \tag{3.9}$$

where ϕ_S is the phase of $M_{\uparrow}$ with respect to microwave field, and the offset $\overline{M}_{\uparrow}$ is given by

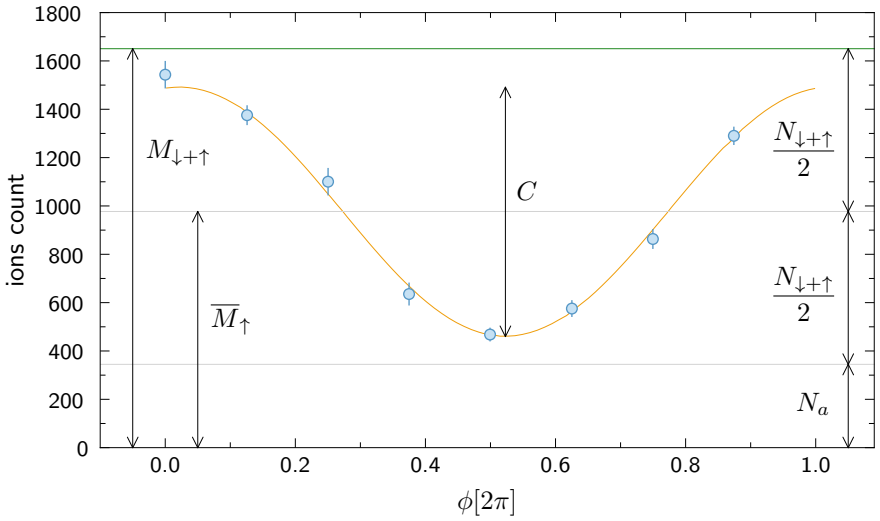

Fig. 3.23 Measurement of the population in the $|\uparrow\rangle$ after a $\pi/2$ readout pulse along angle ϕ in the xy plane according to figure 3.11. $M_{\downarrow+\uparrow}$ is the measurement of the total number of spins. The blue dots represents the mean measurement of

$$\overline{M}_{\uparrow} = \frac{N_{\downarrow+\uparrow}}{2} + N_a. \tag{3.10}$$

From this equations above we can describe the magnetization as a function of the measurements.

$$\langle S(\phi)\rangle = \frac{A}{4\left(M_{\downarrow+\uparrow} - \overline{M}_{\uparrow}\right)} \sin\left(\phi + \phi_S\right) \tag{3.11}$$

The magnetization in the xy plane $\langle S_{xy}\rangle$ of the Bloch-Poincarè sphere can be defined as $\max(\langle S(\phi)\rangle)$, therefore $\langle S_{xy}\rangle = A/\left[4\left(M_{\downarrow+\uparrow} - \overline{M}_{\uparrow}\right)\right]$.

XXZ Rydberg spin system relaxation

Chapter 4

Contents

This chapter is partially based on the following publications, from which parts of the text are reproduced verbatim:

Glassy Dynamics in a Disordered Heisenberg Quantum Spin System A. Signoles, T. Franz, R. Ferracini Alves, M. Gärttner, S. Whitlock, G. Zürn, M. Weidemüller. Physical Review X , Vol. 11, No. 1 (2021)

The author contributed with experimental setup, data acquisition and analysis, simulation of the initial spin distribution, and on the interpretation of the results.

In chapter 2 we demonstrated that an XXZ spin system can be realized by preparing Rydberg atoms in a superposition of $|\downarrow\rangle = |nS\rangle$ and $|\uparrow\rangle = |n'S\rangle$. Chapter 3 shows how this can be achieved experimentally and what are the tools needed to prepare and probe a disordered and isolated XXZ spin system based on cold Rydberg atoms. This chapter goes an important step further and presents experimental results for the relaxations dynamics of interacting Rydberg spin systems.

As discussed in the introduction, understanding the temporal evolution of isolated quantum many body systems is an ongoing challenge in physics [Rigol, Dunjko, and Olshanii, 2008]. Current understanding is that in such systems thermalization occurs through the formation of entanglement [Ueda, 2020]. These theorems describe the steady-state of the system, but a priori no theorem predicts the dynamics of disordered spins towards the equilibrium. This chapter presents the measured magnetization relaxation dynamics in an isolated and disordered XXZ Rydberg spin system to investigate this topic.

Following the experimental procedure detailed in the chapter 2 and summarized in figure 4.1, an ultra-cold gas of ^{87}Rb is excited to a Rydberg spin down state $|\downarrow\rangle \equiv |48S, m_J = +1/2\rangle$, and subsequently put in a superposition with $|\uparrow\rangle \equiv |49S, m_J = +1/2\rangle$ state by a two photon microwave field. The spins interact via Van-der-Waals interactions with $C_6/2\pi = 59\,GHz \times \mu m^6$, and the mean interaction strength between Rydberg atoms are tuned globally by preparing different spin densities. For the experiments described in this thesis, the Wigner-Seitz radius $r_{ws}^0 = (3/4\pi n_S^0)^{1/3}$ for peak Rydberg density n_S^0 ranges from $5.8(5)\,\mu m$

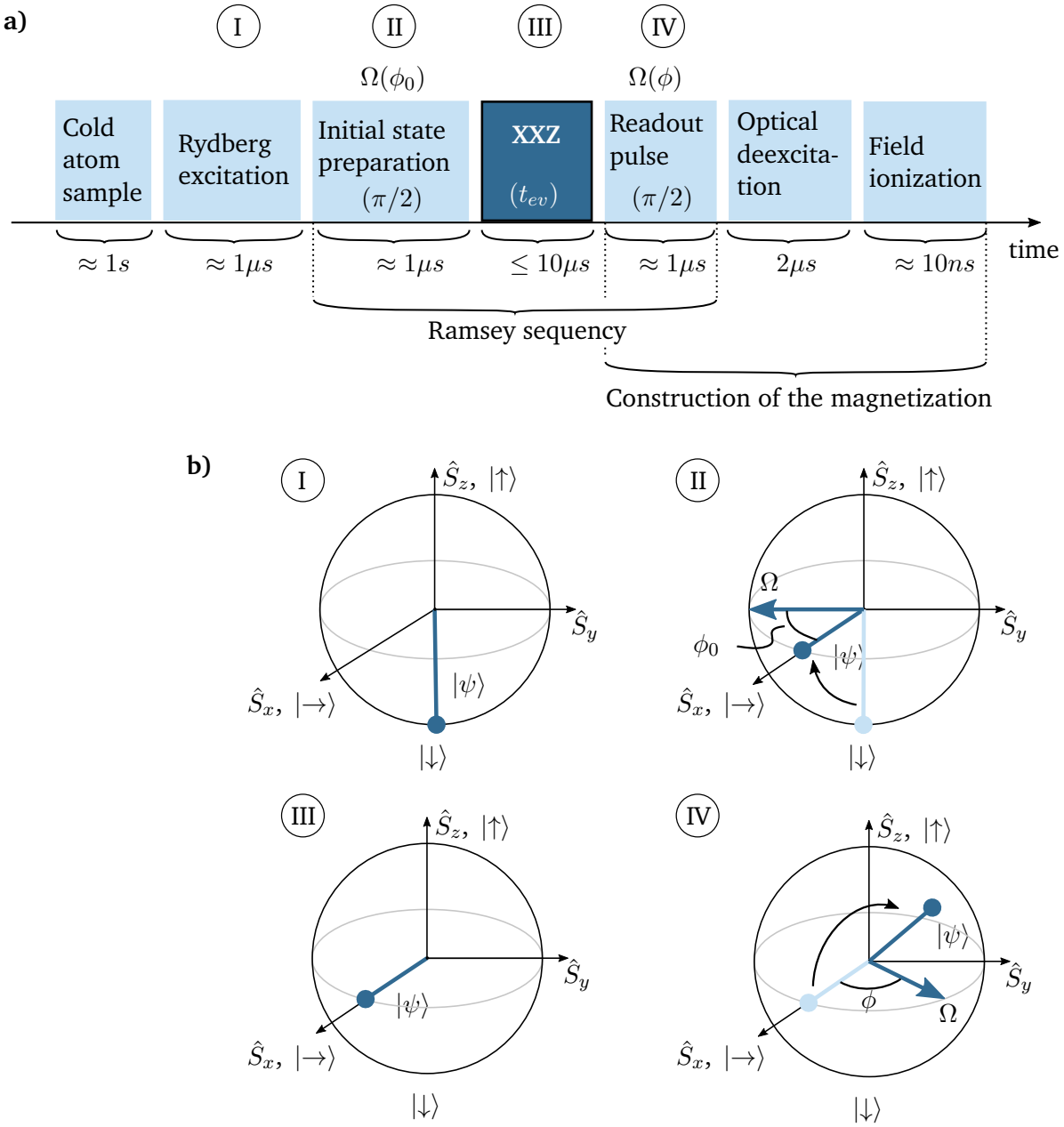

Fig. 4.1 **a)** Heisenberg XXZ experimental sequence for the investigation of the magnetization dynamics. It starts by preparing a cold atom rubidium sample with the target ground state, followed by the Rydberg excitation which creates the total number of spins in the experimental run. The initial state is prepared using a microwave field then a Ramsey sequence where during the free evolution time t_{ev} the atoms evolve through the Heisenberg XXZ unitary dynamics. The second Ramsey pulse has a tunable phase ϕ, and is also part of the process called construction of the magnetization, which adds an optical deexcitation step that depletes all $|\downarrow\rangle$ states, and a Rydberg counting method based on field ionization in order to calculate the magnetization of the system in the xy-plane of the Bloch sphere. **b)** Representation on the Bloch sphere of a few steps on the experimental sequence (indicated by roman numeral in a) and b)). In I - ground state atoms are excited in the $|\downarrow\rangle$ Rydberg spin state; II - a $\pi/2$ pulse in $-y$ direction align the spins towards x direction; III - the interacting spins are allowed a period of free evolution; IV - readout $\pi/2$ pulse with phase ϕ is applied, projecting the desired component of xy-plane onto the z, which is the measurement axis for the optical deexcitation and field ionization steps.

to $8.2(7)\,\mu m$, which leads to a characteristic time scale for the interaction $J_{ij}^0/2\pi = C_6/(2\pi)/(r_{ws}^0)^6$ of $0.7(3)\,\mu s$ to $6(3)\,\mu s$. The lifetime of the states is $56.4\,\mu s$ and $59.6\,\mu s$ for $|48S\rangle$ and $|49S\rangle$ respectively, taking into account the spontaneous decay and black body radiation redistribution at 300 K. Therefore, in order to favor unitary dynamics governed by the Heisenberg spin Hamiltonian, we limit the evolution time to $10\,\mu s$. Before the Rydberg excitation, the cold atomic sample is loaded in an optical dipole trap large compared to the typical blockade radius, which result in a Rydberg ensemble with a 3D spatial geometry.

As the sample is non-degenerate the spatial distribution of the ground state atoms is that of a Maxwell-Boltzmann gas. This disordered distribution is nearly maintained as long as the blockade radius is smaller than the Wigner-Seitz radius. Yet, the blockade radius sets a bound on the minimum distance bellow which no pair of Rydberg atoms is found. Thus the distribution of coupling strengths J_{if} has a maximum bound $J_{max} = (C6/2\pi)/{r_{bl}}^6$. This also sets the scale for the initial dynamics given by pairs with and inter-particle distance equal to the blockade radius.

4.1 Initial state and mean-field predictions

The target initial state for our system is $|{\rightarrow}\rangle_x^{\otimes N} = \left[1/\sqrt{2}\,(|{\uparrow}\rangle + |{\downarrow}\rangle)\right]^{\otimes N}$, which is a interesting choice because it does not show a trivial (mean-field) relaxation. It is clear, if we consider the mean-field XXZ Hamiltonian

$$H_{xxz}^{mf} = \sum_i^N \left(h_x S_x^{(i)} + h_y S_y^{(i)} + h_z \Delta S_z^{(i)}\right) \tag{4.1}$$

with the mean fields $h_\chi = \sum_{j\neq i} J_{ij}\langle S_\chi^{(j)}\rangle$, where χ is either x, y or z, that for the initial state $|{\rightarrow}\rangle_x^{\otimes N}$, the mean field in y and z directions are null and $|{\rightarrow}\rangle_x^{\otimes N}$, is an eigenstate of H_{xxz}^{mf}.

Knowing that the initial state is an eigenstate of the mean field Hamiltonian is important because it accentuates the fact that the relaxation observed in the experiment happens only due to the quantum nature of the spin system. Naturally, proof of unitary dynamics, which will be

demonstrated on section 4.4, is also necessary for this statement to be true.

This distinguishes our experiment from previous reported magnetization relaxation of a driven XY Rydberg spin system by Orioli where mean-field was able to capture all qualitative features of the dynamics [Orioli et al., 2018]. Also, they show that the dephasing of Rabi oscillations could be partially attributed to power fluctuation of the driving field, therefore, the relaxation was also present on the classical picture. Deviations found from mean-field predictions and experimental results were quantitative, rather than qualitative which is the case for the situation presented here.

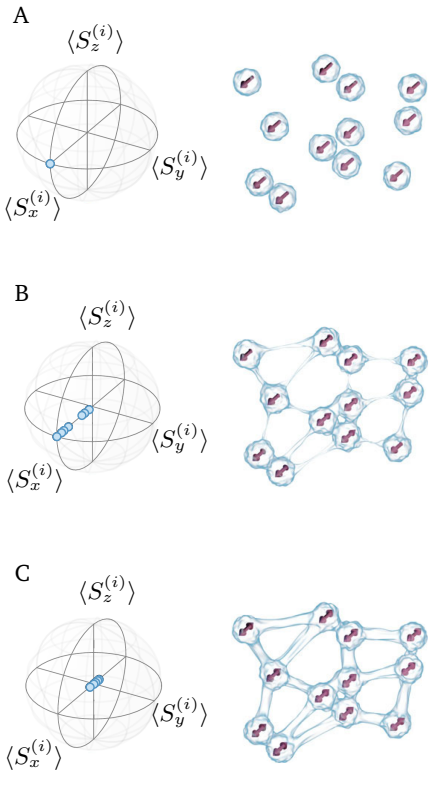

Fig. 4.2: **Building up of entanglement on a disordered few body XXZ spin system. Left:** The microscopic expectation values of $\langle S_x^{(i)}\rangle$, $\langle S_y^{(i)}\rangle$, and $\langle S_z^{(i)}\rangle$ for each spin are plotted at three different time steps on the Bloch sphere for a single disorder realization (gray cuver of figure 4.3). **Right:** Visualization of the reduction of the expectation values (magnetization) as a consequence of the spreading of entanglement represented by the blue bonds between spins).Taken and adapted from Signoles et al., 2021.

4.2 Exact simulation for few particles

To go one step further on our understanding the relaxation dynamics of the disordered XXZ spin system, we realize an exact simulation for 12 spins, distributed in 3D space with uniform random spatial disorder. The relaxation of the magnetization $\langle S_x\rangle_k = 1/N \sum_i \langle S_x^{(i)}\rangle_k$ for a single disorder realization k (gray curve), and the average over 1000 disorder realizations (blue curve) is presented in figure 4.3. The magnetization relaxes to 0 which is in stark contrast with the mean field predictions.

Also shown in figure 4.3 is the second order Rényi entropy, given by

$$\mathcal{S}_i^{(2)} = -\log_2\left[\mathrm{Tr}\left(\rho_i^2\right)\right] \tag{4.2}$$

where $\rho_i = \mathrm{Tr}_{(i)}(\rho)$ is the reduced spin state from the multipartite system with density matrix ρ, where $\mathrm{Tr}_{(i)}$ is the partial trace with respect to the basis of the spin i. The results shows that the system starts in a product state with $\mathcal{S}_i^{(2)} = 0$ and entanglement grows while $\mathcal{S}_i^{(2)}$ reaches its maximum value of 1. For isolated systems, the Renyi entropy is an entanglement measurement, which allow us to confirm for this case our intuition that the relaxation of the magnetization corresponds to a build up of entanglement of the spins.

Even though, we could improve our understanding of the system through the exact few particle simulation, the observations are limited by finite size effects. Considering, for example, that a 3D square grid with 3 spins

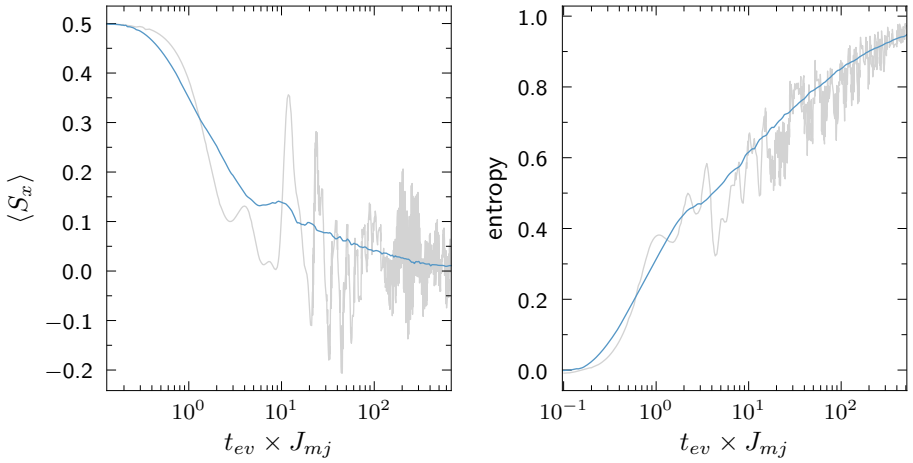

Fig. 4.3 Exact simulation of 12 spins interacting via a Heisenberg XXZ Hamiltonian. **Left:** Magnetization for a single realization (gray curve) and the disorder average over 1000 realizations (blue curve) which relaxes as function of time t_{ev} given in units of the median of the mean-field interaction strengths J_{mf}. **Right:** Buildup of entanglement quantified by the time evolution of the second order Rényi entropy. Ensemble averaged entropy for a single realization (gray curve) and the disorder average over 1000 realizations (blue curve). Since the full system remains pure, the Rényi entropy is a measure of entanglement that increases on similar timescales to the maximal value of $S_i^{(2)} = 1$ as the magnetization relaxes to zero. Taken and adapted from Signoles et al., 2021.

in each direction represents a total of 18 spins and we can only simulate 12 spins in a reasonable time (on a personal computer), it is easy to see that through this route we quickly encounter a computational barrier that prevents us from making an exact simulation of a 3D system. A supercomputer could simulate on the order of 20 spins, which would still show strong finite size effects. With our experimental setup we probe on the order of a thousand Rydberg spins, something impossible to be simulated exactly with current classical numerical computation.

4.3 Discrete Truncated Wigner Approximation

From the previous section, we saw that an exact numerical simulation is not possible for a large number of spins, but there are a few smart numerical approaches that overcome this problem, even though they usually impose a set of restrictions for their applicability [Hazzard et al., 2014]. In particular, we use a numerical method called discrete Truncated Wigner Approximation (dTWA) [Schachenmayer, Pikovski, and A. Rey, 2015], to simulate the full size Rydberg spin system.

The method randomly sample values from the discrete Wigner distribution of the spins initial state and propagates it according to mean-field equations of motion. A Monte-Carlo average from the different initial states sampled is then used to retrieve expectation values. The average of the different trajectories retrieves quantum correlations set by the quantum fluctuations of the initial state, achieving remarkable success when compared to our experimental results (see, for example, figure 4.7).

The dTWA simulations presented in this chapter starts just after the spins excitation step, therefore the initial state is $|\psi_0\rangle = |\downarrow\rangle^{\otimes N}$, but the random sampling of the initial state needs to take into account the uncertainty of each individual spin, which is 1/2 for x and y components (assuming $\hbar = 1$). For the trajectories, we start with the classical spin Hamiltonian

$$H_C = \frac{1}{2}\sum_{i,j,\mu} J_{ij}^{\mu} s_{\mu}^{(i)} s_{\mu}^{(j)} + \sum_{i,\mu} \Omega_{\mu}^{(i)} s_{\mu}^{(i)}, \tag{4.3}$$

with $\mu = (x, y, z)$, $s_{\mu}^{(i)} = \langle S_{\mu}^{(i)} \rangle$, and $\Omega_{\mu}^{(i)}$ is either the Rabi frequency of a driving field if $\mu = x, y$ or the detuning if $\mu = z$. The classical equations of motion for the component of each spin then follow the Hamilton equation

$$\dot{s}_{\mu}^{(i)} = \left\{ H_C, s_{\mu}^{(i)} \right\}. \tag{4.4}$$

4.4 Demonstration of single spin coherence

To ensure unitary evolution of the spin system, we limit the observation time to $10\mu s$, expecting that the decoherence from spontaneous decay ($113\mu s$) and black-body radiation redistribution ($121\mu s$) will not affect the system at this timescale. To prove that this is the case experimentally, and also to make sure the system is not subject to any varying magnetic or electric field that could lead to single spin dephasing, we probe the system in a Ramsey experiment with very low spin density, where we can rule out interaction between the spins.

For this Ramsey sequence, the two $\pi/2$ pulses are applied in phase, and a finite dunning of $\Delta_{mw} = 2\pi \times 0.47MHz$ is used. Therefore, according to equation 3.5, the spins rotate around z direction in the Bloch sphere with a period of $T = 2\pi/\Delta \approx 2\mu s$. The characteristic Ramsey spectroscopy fringes is shown in figure 4.4.

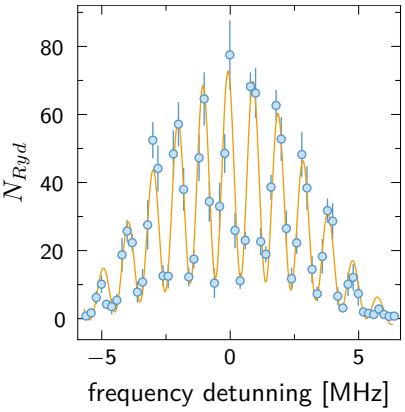

Fig. 4.4 Ramsey fringes measured for the $|48S\rangle$ and $|49S\rangle$ states. The free evolution time between the $\pi/2$ pulses is $1\ \mu s$.

The measured magnetization $\langle S_x \rangle$ as a function of free evolution time t_{ev} is presented in figure 4.6, showing full oscillation during the observation time, which demonstrates a unitary evolution.

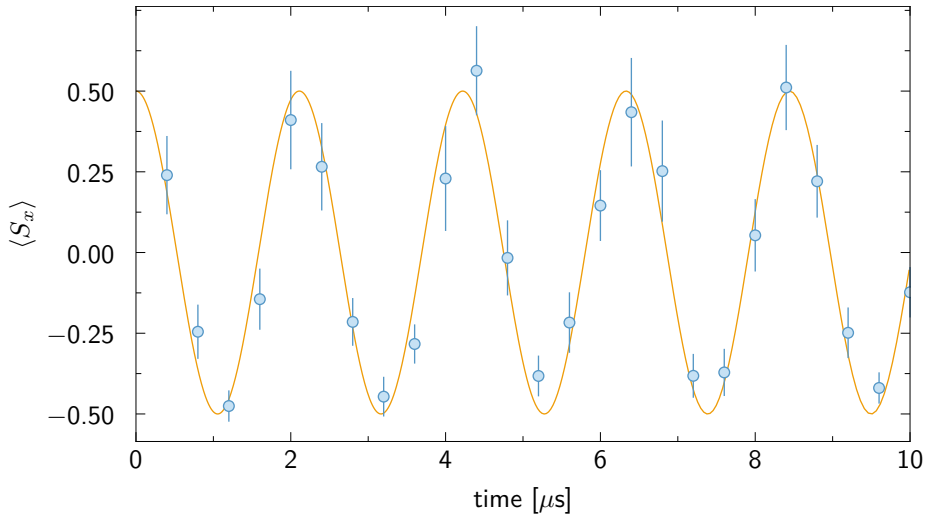

Fig. 4.6 Ramsey oscillations showing high degree of phase coherence for a spin density of $\rho_s^0 = 6.0(15) \times 10^7 cm^{-3}$. Mean results of $\langle S_x \rangle$ measurements are represented by blue dots with error bars showing the standard deviation. The oscillation period correspond to a detunning $\Delta/2\pi = 0.47MHz$. The gray solid line represents a discrete truncated Wigner simulation using the same spin density.

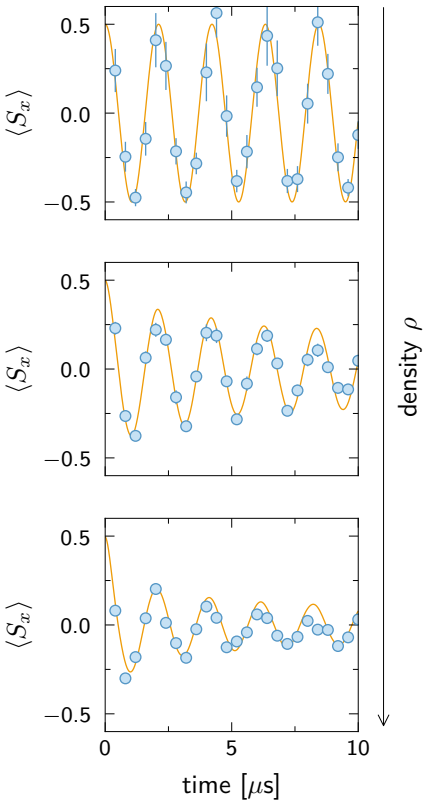

Fig. 4.5 Magnetization relaxation dynamics in a Ramsey interrogation scheme with $\pi/2$ pulses detuned by $\Delta = 2\pi \times 0.47MHz$. Each plot corresponds to a different Rydberg spin density. The blue circles show the temporal evolution of $\langle S_x \rangle$. Orange lines shows dTWA simulation results.

The interaction impact on relaxation of the magnetization $\langle S_x \rangle$ can already be observed in figure 4.4 where we show the magnetization for increasing spin densities. Nevertheless, it was decided to use our tomographic readout scheme to measure the relaxation as it provides not only the magnetization in x direction, but gives access to the full magnetization in the xy plane. Next section presents the relaxation results using the tomographic readout method.

4.5 Slow magnetization relaxation dynamics

In this section we present the results for the measured XXZ relaxation dynamics, which is the main result of this thesis. The experimental procedure follows the description given in the previous chapter. First we excite the spin down state by a two-photon excitation process[see section 3.3], then the state of the atoms is rotated to the targeted initial state, which is the fully magnetized state in the x-direction with $\langle S_x \rangle = 1/2$ by a two-photon spin manipulation field [see section 3.4]. We leave the system under unitary evolution during a time t_{ev} and measure the magnetization by the tomographic technique described in section [see section 3.5].

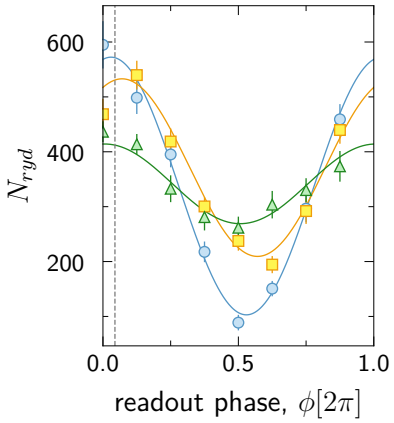

Fig. 4.8 Example of the tomographic readout measurements from where the magnetization $\langle S_x \rangle$ of figure 4.7 was extracted. The blue circles (○) corresponds to $t_{ev} = 0\mu s$, yellow squares (□) to $5\mu s$, and green triangles (△) to $10\mu s$. The symbols represent the mean and error bars the standard error of the mean for total of 15 measurements. The solid lines are a single oscillation fit with amplitude, phase and offset as free parameters. The vertical gray dashed line is showing the mean phase offset for all oscillations.

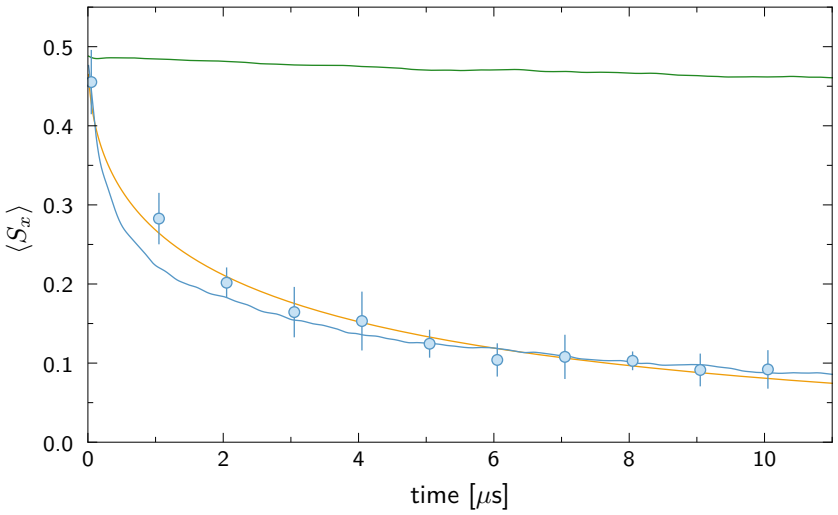

Fig. 4.7 Many-body magnetization dynamics of a XXZ Rydberg spin system. Blue circles (○) show the mean temporal evolution of $\langle S_x \rangle$, and error bars represents standard deviation of 120 measurements with peak spin density of $\rho_S^0 = 1.2(3) \times 10^9 cm^{-3}$. The solid blue line shows the DTWA prediction and the yellow line a fitted stretched exponential curve $1/2e^{-\gamma_J t^\beta}$ with $\beta = 0.32(2)$. The green line shows the mean-field predictions, which deviates significantly from the observed dynamics.

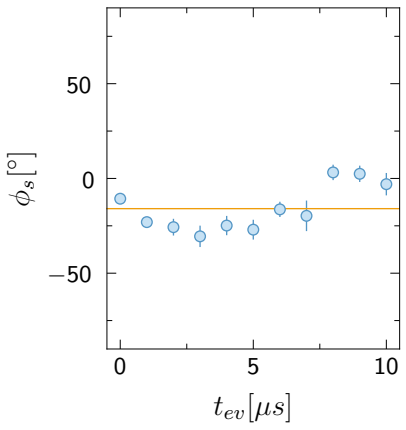

Fig. 4.9 Phase variation of the oscillation fit of the tomographic readout of figure 4.7. The mean phase of - 15.94 degrees is represented by the orange line.

The measured relaxation dynamics of the magnetization is showed in figure 4.7. It shows that the magnetization relaxes to approximately 10% in $10\mu s$, which is much faster than the single spin decoherence, and is in stark contrast to mean-field predictions.

The initial state preparation is not perfect due to fluctuations of the Rabi frequency of the microwave field [Ferreira Cao, 2017], and interactions during the $\pi/2$ pulses [Franz, 2018]. Therefore the mean field relaxation

prediction (green line in figure 4.7) is not completely zero, as one would expect from a pure $|\rightarrow\rangle_x^{\otimes N}$ state (as discussed in section 4.1). Still, even for an imperfect preparation, mean-field relaxation in $10\mu s$ is very small compared to what was measured.

The relaxation was also compared with dTWA simulations (orange line), showing a remarkable agreement. The dTWA simulations had no free parameters, with the exception of the excitation Rabi frequency which was adjusted to give the correct number of Rydberg atoms for each experiment. The small discrepancy between dTWA simulation and experiment might be attributed in a small systematic error on the Rydberg density used in the simulation.

In order to provide a better understanding of the data shown in figure 4.7, a few curves measured by the tomographic readout method are shown in figure 4.8, where each curve corresponds to a different time of figure 4.7. Using a sinusoidal fit the amplitude corresponding to the magnetization in xy-plane is extracted as well as the phase, shown in figure 4.9, from which the magnitude of the x and y component of the magnetization can be extracted.

4.5.1 Slow relaxation of the magnetization

To characterize the measured relaxation dynamics we fit a stretched exponential function

$$\langle S_x \rangle(t) = \frac{1}{2} \exp\left[-\left(\gamma_J\, t\right)^{\beta} \right], \tag{4.5}$$

to the data, with relaxation rate γ_J and stretching exponent β, which typically obtains values between 0 and 1. This phenomenological function has being used for describing the relaxation of complex electronic and molecular systems [Phillips, 1996], and its first application can be attributed to Kohlrausch, 1854. This function has an interesting property, if $\beta = 1$ the relaxation is a simple exponential decay, as β gets lower than 1 the relaxation gets slower. When $\beta \ll 1$ the decay becomes logarithmic, which can be verified by a Taylor expansion of the stretch exponential function

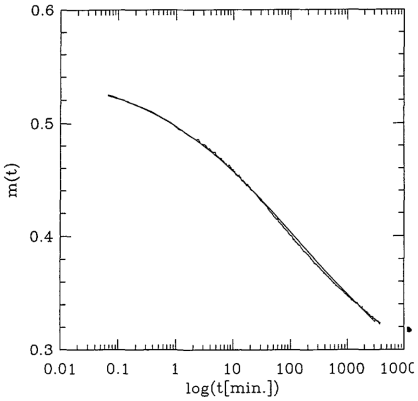

Fig. 4.10 Stretched exponential fit of an aging experiment on $CdCr_{1.7}In_{0.3}S_4$ spin glass. Temperature is 10 Kelvin and initial magnetization 0.567. The stretched exponent is $\beta = 0.24$. Taken from Bouchaud, 1992.

$$\langle S_x \rangle(t) \overset{\beta \ll 1}{=} \frac{1}{2e} - \frac{\beta \log(\gamma_J\, t)}{2e} + \mathcal{O}\left(\beta^3\right). \tag{4.6}$$

The fit of the magnetization measurements presented on figure 4.7 shows a slow relaxation of the magnetization characterized by the stretched exponential fit with $\beta = 0.32(2)$. This slow relaxation is also found in spin glasses, for example, figure 4.10 shows a spin glass aging experiment that was fitted with a stretched exponential. It shows a slow relaxation of the magnetization characterized by a stretched exponent $\beta = 0.24$ [Bouchaud, 1992]. Note that for such experiments, the measurement covers around five decades in time domain, which is beyond what is currently possible in our setup.

Even though the stretched exponential is able to fit well the XXZ experimental relaxation data, from theory we would expect a quadratic behavior at short times. This can be verified by the Baker-Campbell-Haussdorff formula:

$$\begin{aligned} \langle S_x \rangle(t) &= \langle e^{iHt} S_x e^{-iHt} \rangle \\ &= \langle S_x \rangle + it\langle [H, S_x] \rangle - t^2/2 \langle [H, [H, S_x]] \rangle + \ldots \end{aligned} \tag{4.7}$$

For the initial state $|{\rightarrow}\rangle_x^{\otimes N}$, H and S_x commute, which leads the magnetization dynamics to second order in time. It is not the case for the stretched exponential, in this case, if we assume $t \ll 1/\gamma_J$, the stretch exponential assumes a power law function

$$\langle S_x \rangle(t) = 1/2 \left[1 - \beta(\gamma_J t)^\beta\right]. \tag{4.8}$$

For this reason we exclude the first data point from our fitting. Nevertheless, the resulting curve actually fits well all data points, including the first measurement of the magnetization.

4.6 Role of disorder in the relaxation

One question one might ask is how the disorder in the system affects the stretched exponent β. To investigate this issue we repeated the relaxation experiment for different densities, keeping the excitation

volume constant, and varying peak density ρ_S^0 by applying different excitation times t_{exc}. Each density can be associated to a corresponding pair distance called Wigner-Seitz radius, given by

$$a_0 = \sqrt[3]{\frac{3}{4\pi\rho_S^0}}. \tag{4.9}$$

Without the Rydberg blockade effect, the nearest neighbor distance distribution associated with each a_0 is [Hertz, 1909]

$$h(r) = \frac{3r^2}{a_0^3} \exp\left[-\left(\frac{r}{a_0}\right)^3\right], \tag{4.10}$$

with associated interaction distribution $h(J) = h(r)\,(\partial r/\partial J)$. But the blockade effect, introduces a cutoff to the minimum pair distance R_{bl}, which also impacts the interaction strength distribution. Let's define $g(J)$ the real interaction strength distribution accounting for the Rydberg blockade as shown in figure 4.6, we can then measure how different is $g(J)$ from our reference probability distribution $h(J)$ using the relative entropy called Kullback–Leibler divergence, given by [Kullback and Leibler, 1951]

$$\mathcal{D}_{kl}\,(g||h) = \int g(J) \log\left(\frac{g(J)}{h(J)}\right) dJ, \tag{4.11}$$

which gives a positive value that increases with the gain in information of $g(J)$ relative to $h(J)$. Figure 4.6 shows that for uniform distributions, $\mathcal{D}_{kl}$ increases monotonically with $(a_0/R_{bl})^{-3}$, indicating the ratio of the Wigner-Seitz radius and the Rydberg blockade can be used as a measure of disorder strength.

Figure 4.14 shows the magnetization relaxation for different densities. Important parameters for each of the datasets presented are listed in table 4.1. For each density we fit a stretch exponential, as described in equation 4.5. We first allow β to vary as a free parameter (solid gray line), and also plot a pure exponential fit (light gray dotted dash line) and a stretch exponential with fixed $\beta = 0.5$ for comparison.

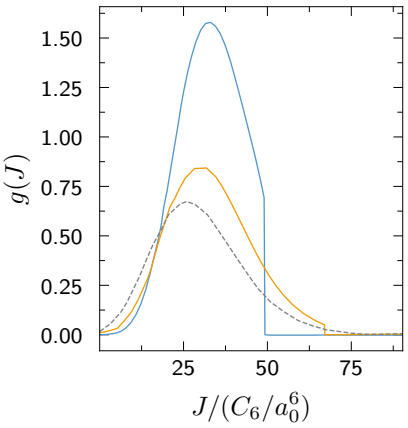

Fig. 4.11 Normalized probability distribution of nearest-neighbor interactions $g(J)$ for different homogeneous spin densities (blue line, $\rho_S = 2.11 \times 10^9\,cm^{-3}$; orange line, $\rho_S = 8.73 \times 10^8\,cm^{-3}$). The dashed line depicts a distribution corresponding to randomly placed spins. The blockade effect induces correlations in the system and hence the probability distribution at high densities becomes more peaked. This results in a decreased disorder compared to the completely random case. Taken and adapted from Signoles et al., 2021.

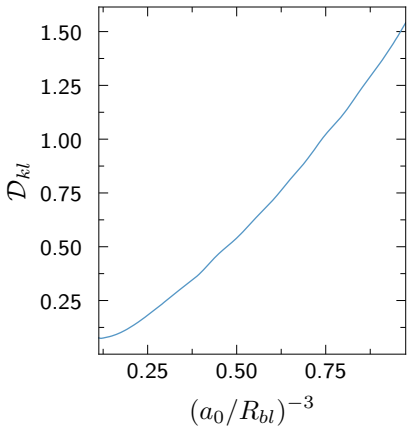

Fig. 4.12 Scaling of the disorder strength as a function of density. The Kullback-Leibler divergence DKL increases monotonically with $(a_0/R_{bl})^{-3}$. Simulation done for a uniform distribution. Taken and adapted from Signoles et al., 2021.

Figure marker	○	□	△	◇
$t_{exc}[\mu s]$	0.6	0.8	1.0	1.0
$\rho^0_{gs}[10^{11}\,cm^{-3}]$	1.69(12)	1.73(9)	1.64(15)	1.79(9)
$\rho^0_S[10^9\,cm^{-3}]$	0.43(11)	0.8(2)	1.1(3)	1.2(3)
$N_S[10^3]$	0.4(1)	0.8(2)	1.2(3)	1.2(3)
$R_{bl}[\mu m]$	4.81	5.03	5.21	5.21
$a_0[\mu m]$	8.2(7)	6.6(6)	5.9(5)	5.8(5)
$(a_0/R_{bl})^{-3}$	0.20(5)	0.43(11)	0.7(2)	0.7(2)
$C_6/(2\pi)/a_0^6[MHz]$	0.195(97)	0.7(3)	1.4(7)	1.5(8)
β	0.37(2)	0.36(4)	0.305(14)	0.32(2)

Tab. 4.1 Experimental parameters. t_{exc} denotes the time of laser excitation from the ground to the Rydberg state. ρ^0_{gs} denotes the measured ground-state density. ρ^0_S the derived peak spin density, N_S the derived number of total spins. R_{bl} is the blockade radius derived from the excitation time and laser coupling strength. a_0 denotes the Wigner-Seitz radius, C_6 the van der Waals coefficient, and β is the exponent of the stretching exponential derived from a fit to the relaxation curves. Taken and adapted from Signoles et al., 2021.

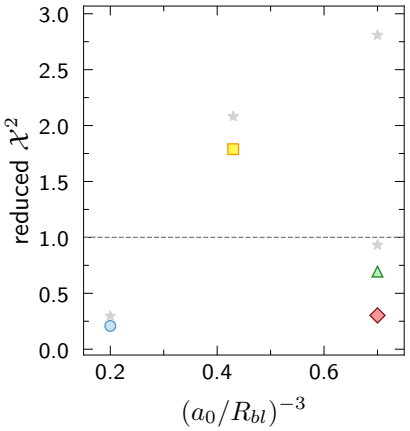

Fig. 4.13 Reduced $\mathcal{X}^2$ as a function of $(a_0/R_{bl})^{-3}$ for each magnetization relaxation measurement set. The each symbol matches the corresponding measurements on figure 4.14. Just for the second dataset (yellow) the reduced $\mathcal{X}^2$ is bigger than one, but not by much. Therefore, we assume the stretched exponential is in general describing well the relaxation measurements. The grey stars shows the reduced $\mathcal{X}^2$ for the fixed $\beta = 0.5$ curves.

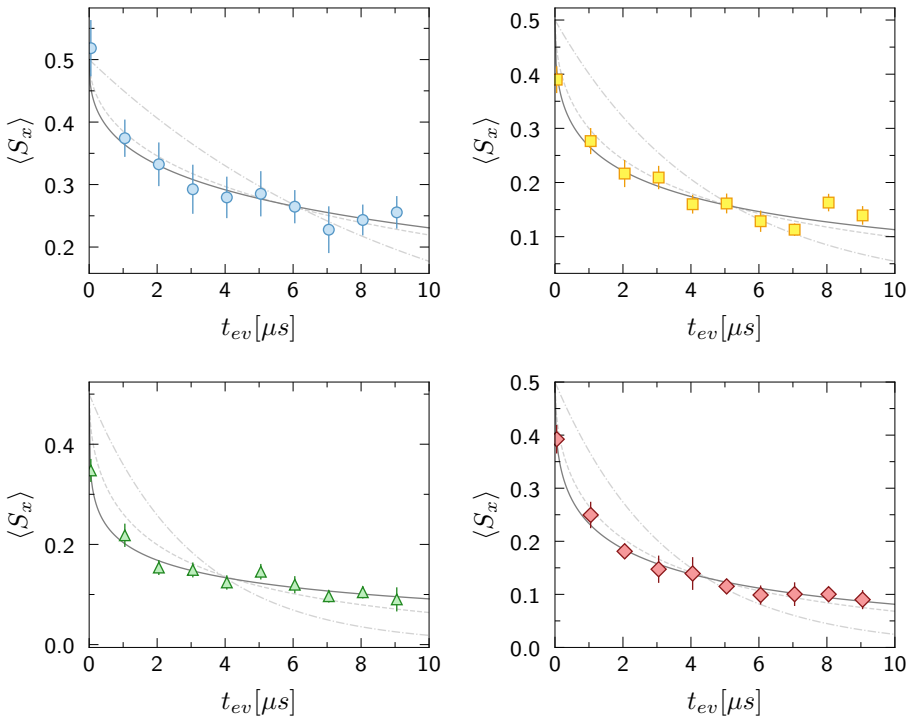

Fig. 4.14 Data points represent measurements of the averaged magnetization $\langle S_x \rangle$ for spin densities $\rho^0_S = 0.43(11) \times 10^9\,cm^{-3}$ (blue circles ○), $0.8(2) \times 10^9 cm^{-3}$ (yellow squares □), and $1.2(3) \times 10^9 cm^{-3}$ (both for green triangles △ and red diamond markers ◇) with respect to XXZ free interaction time t_{ev}. The solid gray lines for each figure shows the stretched exponential fit of equation 4.5. For comparison, the dashed light gray line shows a stretched exponential fit with fixed $\beta = 1/2$, and dashed dot line a pure exponential decay ($\beta = 1$).

In order to quantify the quality of the fitting curves, figure 4.13 shows the reduced $\mathcal{X}^2$ for each of the datasets [1]. It shows that, with exception of the relaxation curve for $\rho_S^0 = 0.8(2) \times 10^9 cm^{-3}$ (■), the relaxation measurements are fitted well with a stretched exponential, where the reduced $\mathcal{X}^2 < 2$ for all datasets.

From figure 4.15 it is possible to conclude that there is no experimental evidence pointing towards a change in β for the disorder range probed in our experiment.

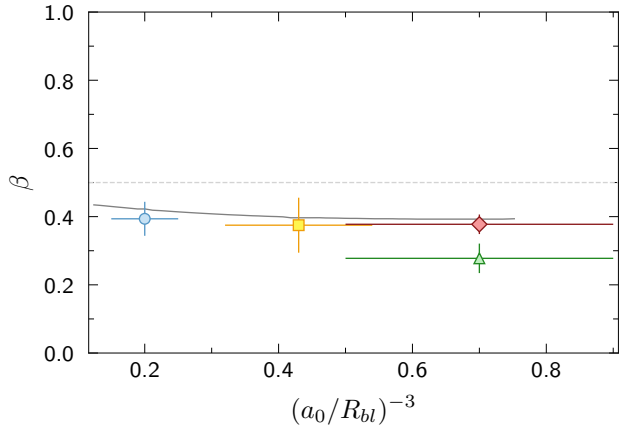

Fig. 4.15 Data points represent the stretched exponent β as a function of $(a_0/R_{bl})^{-3}$ for each of the four magnetization relaxation measurements. The solid gray line represents dTWA simulations, and the dashed line shows $\beta = 0.5$ as a reference to the eye.

[1] the reduced $\mathcal{X}^2$ is given by

$$\text{red.}\,\mathcal{X}^2 = \frac{\sum_{i=1}^{N} r_i^2/\sigma_i^2}{N - N_{var}}, \qquad (4.12)$$

where N is the number of datapoints, N_{var} the number of fitting variables, r_i the residuals, and σ_i the standard deviation of the data.

4.7 Re-scaling of time for datasets with different spin densities

In the last section we showed that there was no expressive variation of the stretched exponent for different spin densities. Therefore, it should be possible to re-scale time in order to create a larger data set expanding our measurement range beyond a single decade. The result is shown in figure 4.16 where the re-scaling was done using the interaction strength given by $(a_0/R_{bl})^{-3}$.

As we cover 2 orders of magnitude in re-scaled time and extracted a β of 0.32 which is significantly smaller than 1, we can clearly state that the system relaxes sub-exponentially and shows a relaxation behavior similar to what has been found in spin-glasses.

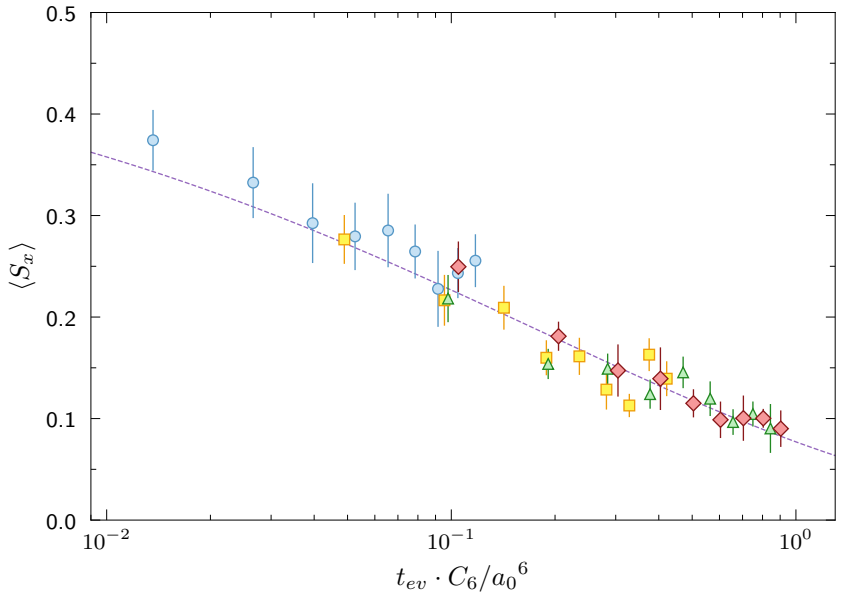

Fig. 4.16 Data points shows the magnetization $\langle S_x \rangle$ as a function of the re-scaled time using the effective interaction strength C_6/a_0^6 for all datasets used in figure 4.14 and represented in table 4.1. After re-scaling the datasets corresponding to different densities all follow a single stretched exponential function with $\beta = 0.32(2)$ and reduced $\mathcal{X}^2$ of 0.97 (dashed purple line).

This analysis shows clearly, that the blockade radius changes the microscopic details of the system, but it does not change the macroscopic relaxation dynamics. An intuitive understanding for this behavior might be that the blockade radius only affects strongly interacting spins that relax fast and don't contribute to the late time dynamics that is described by the stretched exponential function. On the basis of this observation, we assume that stretched exponential relation is a general feature of disordered spin systems. Indeed, numerical investigations of uniform distributions of spins show exactly the same behavior including the insensitivity with respect to the blockade radius. It also shows that if we extrapolate the results for higher ordering systems the slow dynamics regime breaks down [Signoles et al., 2021].

Chapter 5

Conclusion

In this thesis we started by demonstrating how Rydberg systems can be mapped to different spin 1/2 Hamiltonians, and showed that a system comprised of atoms in two Rydberg states with no orbital angular momentum $|nS\rangle$ and $|n'S\rangle$ can be mapped onto an XXZ spin system. Some important aspects of Rydberg atoms such as the finite lifetime were discussed. We showed that for the chosen states, $|48S\rangle$ and $|49S\rangle$, both spontaneous decay and black-body radiation coupling limit the Rydberg spins lifetime in equal measure, yet not compromising the spin dynamics which happens on timescales orders of magnitude faster then the lifetime.

We also described how such an XXZ spin system based on Rydberg atoms can be realized experimentally using cold Rubidium atoms. We isolated an effective two-level system in the Rydberg manifold which is coupled by two-photon transitions using microwave radiation and showed that unwanted population in other Rydberg states is as small as a few percent. For sufficient cooling the ensemble of Rydberg atoms can be considered as a frozen gas, i.e. the particles move far less then mean inter-particle distance within the typical experimental timescales and therefore the mapping to a spin system can be applied. We experimentally showed that the single spin coherence time is much longer then the timescale set by the interaction of the Rydberg spins allowing to investigate unitary evolution up to $10\mu s$.

The successful experimental implementation of the Rydberg spin system enabled us to study the out-of-equilibrium dynamics of a disordered Heisenberg XXZ system. After unitary Hamiltonian evolution we probed the magnetization of the Rydberg spin system as function of time. We showed that for the chosen initial product state with all spins pointing in x-direction there is no dynamics according to the classical equation of motion. Therefore the we could attributed the observed relaxation dynamics to the quantum nature of the spin-system. The experiment follows exact numerical simulation of a few spins, where the relaxation correlates with the build up of entanglement in the system.

The measurement of the relaxation of the magnetization has been fitted with a phenomenological stretched exponential function, also used to characterized slow relaxation in spin glasses. We find a stretched exponent of 0.32 which indeed reveals a slow relaxation of the Rydberg spin system. We found no significant variation of the stretched exponential with the different degrees of disorder we could probe with our setup. This hints towards universality of this exponent since it is insensitive to the microscopic details of the spins arrangement. Also it allowed us to scale the temporal axis, in our case by the van der Waals interaction energy given by the Wigner-Seitz radius, which then created an extended set of data for the relaxation dynamics that spanned for two decades showing that the slow relaxation is not only a transient effect but persists for long times. The experimental data for the XXZ spin relaxation was compared to Discrete Truncated Wigner Approximation simulations, showing great agreement. This success of the simulation stimulated us to simulate the relaxation dynamics for degrees of order that could not be achieved in our experiment. This numerical exploration indicates that for systems above a certain degree of order the universal behavior observed in the disordered regime breaks down.

Bibliography

Altman, Ehud et al. “Quantum Simulators: Architectures and Opportunities”. In: *PRX Quantum* 2.1 (Feb. 2021), p. 017003. DOI: 10.1103/prxquantum.2.017003.

Anderson, P. W. “More is Different: Broken Symmetry and the Nature of the Hierarchical Structure of Science”. In: *Emergence*. The MIT Press, Mar. 2008, pp. 221–230. DOI: 10.7551/mitpress/9780262026215.003.0013.

Bardeen, J., L. N. Cooper, and J. R. Schrieffer. “Theory of Superconductivity”. In: *Physical Review* 108.5 (Dec. 1957), pp. 1175–1204. DOI: 10.1103/physrev.108.1175.

Barredo, Daniel, Sylvain de Léséleuc, et al. “An atom-by-atom assembler of defect-free arbitrary two-dimensional atomic arrays”. In: *Science* 354.6315 (Nov. 2016), pp. 1021–1023. DOI: 10.1126/science.aah3778.

Barredo, Daniel, Vincent Lienhard, et al. “Synthetic three-dimensional atomic structures assembled atom by atom”. In: *Nature* 561.7721 (Sept. 2018), pp. 79–82. DOI: 10.1038/s41586-018-0450-2.

Bernien, Hannes et al. “Probing many-body dynamics on a 51-atom quantum simulator”. In: *Nature* 551.7682 (Nov. 2017), pp. 579–584. DOI: 10.1038/nature24622.

Bilitewski, Thomas et al. “Dynamical Generation of Spin Squeezing in Ultracold Dipolar Molecules”. In: *Physical Review Letters* 126.11 (Mar. 2021), p. 113401. DOI: 10.1103/physrevlett.126.113401.

Bloch, Immanuel, Jean Dalibard, and Sylvain Nascimbène. “Quantum simulations with ultracold quantum gases”. In: *Nature Physics* 8.4 (Apr. 2012), pp. 267–276. DOI: 10.1038/nphys2259.

Bohn, John L., Ana Maria Rey, and Jun Ye. “Cold molecules: Progress in quantum engineering of chemistry and quantum matter”. In: *Science* 357.6355 (Sept. 2017), pp. 1002–1010. DOI: 10.1126/science.aam6299.

Bouchaud, J. P. “Weak ergodicity breaking and aging in disordered systems”. In: *Journal de Physique I* 2.9 (Sept. 1992), pp. 1705–1713. DOI: 10.1051/jp1:1992238.

Browaeys, Antoine and Thierry Lahaye. “Many-body physics with individually controlled Rydberg atoms”. In: *Nature Physics* 16.2 (Jan. 2020), pp. 132–142. DOI: 10.1038/s41567-019-0733-z.

Busche, Hannes. “Efficient loading of a magneto-optical trap for experiments with dense ultracold Rydberg gases”. MA thesis. University Library Heidelberg, 2011.

Choi, Joonhee et al. “Depolarization Dynamics in a Strongly Interacting Solid-State Spin Ensemble”. In: *Physical Review Letters* 118.9 (Mar. 2017), p. 093601. DOI: 10.1103/physrevlett.118.093601.

Coleman, Piers. *Introduction to many body physics*. New York, NY: Cambridge University Press, 2015. ISBN: 9781139020916.

Comparat, Daniel and Pierre Pillet. “Dipole blockade in a cold Rydberg atomic sample [Invited]”. In: *Journal of the Optical Society of America B* 27.6 (June 2010), A208. DOI: 10.1364/josab.27.00a208.

Ebadi, Sepehr et al. “Quantum phases of matter on a 256-atom programmable quantum simulator”. In: *Nature* 595.7866 (July 2021), pp. 227–232. DOI: 10.1038/s41586-021-03582-4.

Endres, Manuel et al. “Atom-by-atom assembly of defect-free one-dimensional cold atom arrays”. In: *Science* 354.6315 (Nov. 2016), pp. 1024–1027. DOI: 10.1126/science.aah3752.

Ferreira Cao, Miguel. “Control and characterisation of a Rydberg spin system to explore many-body physics”. PhD thesis. 2017. DOI: 10.11588/HEIDOK.00023769.

Ferreira Cao, Miguel et al. “Depletion imaging of Rydberg atoms in cold atomic gases”. In: *Journal of Physics B: Atomic, Molecular and Optical Physics* 53.8 (Mar. 2020), p. 084004. DOI: 10.1088/1361-6455/ab7427.

Feynman, Richard P. “Simulating physics with computers”. In: *International Journal of Theoretical Physics* 21.6-7 (June 1982), pp. 467–488. DOI: 10.1007/bf02650179.

Foot, Christopher J. *Atomic Physics*. Oxford University Press, Jan. 2005. 346 pp. ISBN: 0198506961.

Franz, Titus. “Quantum simulation of relaxation dynamics of a Heisenberg Hamiltonian using Rydberg spins”. MA thesis. Heidelberg University, 2018.

Gaëtan, Alpha et al. “Observation of collective excitation of two individual atoms in the Rydberg blockade regime”. In: *Nature Physics* 5.2 (Jan. 2009), pp. 115–118. DOI: 10.1038/nphys1183.

Gallagher, Thomas. *Rydberg atoms*. Cambridge New York: Cambridge University Press, 1994. ISBN: 9780521385312.

Glaetzle, A. W. et al. “A coherent quantum annealer with Rydberg atoms”. In: *Nature Communications* 8.1 (June 2017). DOI: 10.1038/ncomms15813.

Günter, Georg Gotthilf. “Interfacing Rydberg atoms with light and observing their interaction driven dynamics”. PhD thesis. 2014. DOI: 10.11588/HEIDOK.00016312.

Harold J. Metcalf, Peter van der Straten. *Laser Cooling and Trapping*. Springer New York, Dec. 2012. 324 pp. ISBN: 9781461214700.

Hazzard, Kaden R. A. et al. “Many-Body Dynamics of Dipolar Molecules in an Optical Lattice”. In: *Physical Review Letters* 113.19 (Nov. 2014), p. 195302. DOI: 10.1103/physrevlett.113.195302.

Hertz, Paul. “Über den gegenseitigen durchschnittlichen Abstand von Punkten, die mit bekannter mittlerer Dichte im Raume angeordnet sind”. In: *Mathematische Annalen* 67.3 (Sept. 1909), pp. 387–398. DOI: 10.1007/bf01450410.

Hofmann, C. S. et al. “An experimental approach for investigating many-body phenomena in Rydberg-interacting quantum systems”. In: *Frontiers of Physics* 9.5 (Nov. 2013), pp. 571–586. DOI: 10.1007/s11467-013-0396-7.

Höltkemeier, Bastian. *2D MOT as a source of a cold atom target*. 2011.

Isenhower, L. et al. “Demonstration of a Neutral Atom Controlled-NOT Quantum Gate”. In: *Physical Review Letters* 104.1 (Jan. 2010), p. 010503. DOI: 10.1103/physrevlett.104.010503.

Kaplan, Harvey B. et al. “Many-Body Dephasing in a Trapped-Ion Quantum Simulator”. In: *Physical Review Letters* 125.12 (Sept. 2020), p. 120605. DOI: 10.1103/physrevlett.125.120605.

Keesling, Alexander et al. “Quantum Kibble–Zurek mechanism and critical dynamics on a programmable Rydberg simulator”. In: *Nature* 568.7751 (Apr. 2019), pp. 207–211. DOI: 10.1038/s41586-019-1070-1.

King, B. E. “Angular Momentum Coupling and Rabi Frequencies for Simple Atomic Transitions”. In: (Apr. 29, 2008). arXiv: 0804.4528 [physics.atom-ph].

Kohlrausch, R. “Theorie des elektrischen Rückstandes in der Leidener Flasche”. In: 167.2 (1854), pp. 179–214. DOI: 10.1002/andp.18541670203.

Kullback, S. and R. A. Leibler. “On Information and Sufficiency”. In: *The Annals of Mathematical Statistics* 22.1 (Mar. 1951), pp. 79–86. DOI: 10.1214/aoms/1177729694.

Labuhn, Henning et al. “Tunable two-dimensional arrays of single Rydberg atoms for realizing quantum Ising models”. In: *Nature* 534.7609 (June 2016), pp. 667–670. DOI: 10.1038/nature18274.

Landau, L. “Theory of the Superfluidity of Helium II”. In: *Physical Review* 60.4 (Aug. 1941), pp. 356–358. DOI: 10.1103/physrev.60.356.

Lanyon, B. P. et al. “Efficient tomography of a quantum many-body system”. In: *Nature Physics* 13.12 (Sept. 2017), pp. 1158–1162. DOI: 10.1038/nphys4244.

Li, Wenhui et al. “Millimeter-wave spectroscopy of cold Rb Rydberg atoms in a magneto-optical trap: Quantum defects of thens,np, andndseries”. In: *Physical Review A* 67.5 (May 2003), p. 052502. DOI: 10.1103/physreva.67.052502.

Löw, Robert et al. “An experimental and theoretical guide to strongly interacting Rydberg gases”. In: *Journal of Physics B: Atomic, Molecular and Optical Physics* 45.11 (May 2012), p. 113001. DOI: 10.1088/0953-4075/45/11/113001.

Lucas, Andrew. “Ising formulations of many NP problems”. In: *Frontiers in Physics* 2 (2014). DOI: 10.3389/fphy.2014.00005.

Marinescu, M., H. R. Sadeghpour, and A. Dalgarno. “Dispersion coefficients for alkali-metal dimers”. In: *Physical Review A* 49.2 (Feb. 1994), pp. 982–988. DOI: 10.1103/physreva.49.982.

Martinson, I. and L.J. Curtis. “Janne Rydberg – his life and work”. In: *Nuclear Instruments and Methods in Physics Research Section B: Beam Interactions with Materials and Atoms* 235.1-4 (July 2005), pp. 17–22. DOI: 10.1016/j.nimb.2005.03.137.

Monroe, C. et al. “Programmable quantum simulations of spin systems with trapped ions”. In: *Reviews of Modern Physics* 93.2 (Apr. 2021), p. 025001. DOI: 10.1103/revmodphys.93.025001.

Müller, Nele Lotte Marie. “Excitation and Detection of Rydberg Atomsin an Ultracold Gas”. MA thesis. Heidelberg Univeristy, 2010.

Orioli, A. Piñeiro et al. “Relaxation of an Isolated Dipolar-Interacting Rydberg Quantum Spin System”. In: 120.6 (Feb. 2018), p. 063601. DOI: 10.1103/physrevlett.120.063601.

Parkinson, John and Damian J J Farnell. *An Introduction to Quantum Spin Systems*. Springer Berlin Heidelberg, 2010. DOI: 10.1007/978-3-642-13290-2.

Paz, A. de et al. “Nonequilibrium Quantum Magnetism in a Dipolar Lattice Gas”. In: *Physical Review Letters* 111.18 (Oct. 2013), p. 185305. DOI: 10.1103/physrevlett.111.185305.

Phillips, J C. “Stretched exponential relaxation in molecular and electronic glasses”. In: 59.9 (Sept. 1996), pp. 1133–1207. DOI: 10.1088/0034-4885/59/9/003.

Rau, A. R. P. and Mitio Inokuti. “The quantum defect: Early history and recent developments”. In: *American Journal of Physics* 65.3 (Mar. 1997), pp. 221–225. DOI: 10.1119/1.18532.

Rigol, Marcos, Vanja Dunjko, and Maxim Olshanii. “Thermalization and its mechanism for generic isolated quantum systems”. In: 452.7189 (Apr. 2008), pp. 854–858. DOI: 10.1038/nature06838.

Robicheaux, F. and J. V. Hernández. “Many-body wave function in a dipole blockade configuration”. In: *Physical Review A* 72.6 (Dec. 2005), p. 063403. DOI: 10.1103/physreva.72.063403.

Ryabtsev, I. I. et al. “Observation of the Stark-Tuned Förster Resonance between Two Rydberg Atoms”. In: *Physical Review Letters* 104.7 (Feb. 2010), p. 073003. DOI: 10.1103/physrevlett.104.073003.

Sachdev, Subir. *Quantum Phase Transitions*. Cambridge University Press, Mar. 2017. 520 pp. ISBN: 0521514681.

Sansonetti, Jean. *Handbook of Basic Atomic Spectroscopic Data, NIST Standard Reference Database 108*. en. 2003. DOI: 10.18434/T4FW23.

Schachenmayer, J., A. Pikovski, and A. M. Rey. "Many-Body Quantum Spin Dynamics with Monte Carlo Trajectories on a Discrete Phase Space". In: *Physical Review X* 5.1 (Feb. 2015), p. 011022. DOI: 10.1103/physrevx.5.011022.

Schauß, P. et al. "Crystallization in Ising quantum magnets". In: *Science* 347.6229 (Mar. 2015), pp. 1455–1458. DOI: 10.1126/science.1258351.

Schauss, Peter. "Quantum simulation of transverse Ising models with Rydberg atoms". In: *Quantum Science and Technology* 3.2 (Jan. 2018), p. 023001. DOI: 10.1088/2058-9565/aa9c59.

Seaton, M J. "Quantum defect theory". In: *Reports on Progress in Physics* 46.2 (Feb. 1983), pp. 167–257. DOI: 10.1088/0034-4885/46/2/002.

Šibalić, N. et al. "ARC: An open-source library for calculating properties of alkali Rydberg atoms". In: *Computer Physics Communications* 220 (Nov. 2017), pp. 319–331. DOI: 10.1016/j.cpc.2017.06.015.

Signoles, A. et al. "Glassy Dynamics in a Disordered Heisenberg Quantum Spin System". In: *Physical Review X* 11.1 (Jan. 2021), p. 011011. DOI: 10.1103/physrevx.11.011011.

Singer, Kilian et al. "Long-range interactions between alkali Rydberg atom pairs correlated to thens–ns,np–np andnd–nd asymptotes". In: *Journal of Physics B: Atomic, Molecular and Optical Physics* 38.2 (Jan. 2005), S295–S307. DOI: 10.1088/0953-4075/38/2/021.

Smith, Adam et al. "Simulating quantum many-body dynamics on a current digital quantum computer". In: *npj Quantum Information* 5.1 (Nov. 2019). DOI: 10.1038/s41534-019-0217-0.

Stanojevic, J. and R. Côté. "Many-body Rabi oscillations of Rydberg excitation in small mesoscopic samples". In: *Physical Review A* 80.3 (Sept. 2009), p. 033418. DOI: 10.1103/physreva.80.033418.

Steck, Daniel Adam. "Rubidium 87 D Line Data". In: 2021.

Tang, Yijun et al. "Thermalization near Integrability in a Dipolar Quantum Newton's Cradle". In: *Physical Review X* 8.2 (May 2018), p. 021030. DOI: 10.1103/physrevx.8.021030.

Ueda, Masahito. "Quantum equilibration, thermalization and prethermalization in ultracold atoms". In: 2.12 (Oct. 2020), pp. 669–681. DOI: 10.1038/s42254-020-0237-x.

Urban, E. et al. "Observation of Rydberg blockade between two atoms". In: *Nature Physics* 5.2 (Jan. 2009), pp. 110–114. DOI: 10.1038/nphys1178.

Venturelli, Davide et al. "Quantum Optimization of Fully Connected Spin Glasses". In: *Physical Review X* 5.3 (Sept. 2015), p. 031040. DOI: 10.1103/physrevx.5.031040.

Weber, Sebastian et al. "Calculation of Rydberg interaction potentials". In: *Journal of Physics B: Atomic, Molecular and Optical Physics* 50.13 (June 2017), p. 133001. DOI: 10.1088/1361-6455/aa743a.

Wilk, T. et al. "Entanglement of Two Individual Neutral Atoms Using Rydberg Blockade". In: *Physical Review Letters* 104.1 (Jan. 2010), p. 010502. DOI: 10.1103/physrevlett.104.010502.

Zeiher, Johannes. "Realization of Rydberg-dressed quantum magnets". PhD thesis. Ludwig Maximilians Universität, 2017. eprint: http://hdl.handle.net/21.11116/0000-0001-47D3-1.

Zeiher, Johannes, Rick van Bijnen, et al. "Many-body interferometry of a Rydberg-dressed spin lattice". In: *Nature Physics* 12.12 (Aug. 2016), pp. 1095–1099. DOI: 10.1038/nphys3835.

Zeiher, Johannes, Jae-yoon Choi, et al. "Coherent Many-Body Spin Dynamics in a Long-Range Interacting Ising Chain". In: *Physical Review X* 7.4 (Dec. 2017), p. 041063. DOI: 10.1103/physrevx.7.041063.

Zeiher, Johannes, Peter Schauß, et al. “Microscopic Characterization of Scalable Coherent Rydberg Superatoms”. In: *Physical Review X* 5.3 (Aug. 2015), p. 031015. DOI: 10.1103/physrevx.5.031015.

Acknowledgement

In this last section, I would like to share my gratitude to all people that helped along my doctorate journey.

First I would like to share gratitude to my supervisor **Prof. Dr. Matthias Weidemüller**. Thank you for giving me the opportunity of joining the Rydberg team, and contribute to exciting experiments. It was a lifelong dream you helped me to fulfill. Thank you also for your supporting me along the way, and helping me with my doctorate activities and beyond.

I'm grateful to **Prof. Dr. Jörg Evers** for accepting to be the second referee for this thesis and for taking part in my examination. And I would also like to thank **Prof. Dr. Selim Jochim** and **Priv.-Doz. Dr. Martin Gärttner** who kindly accepted to evaluate my doctoral defense.

Let me share my deepest gratitude to **Dr. Gerhard Zürn**. I was lucky to get your guidance since the beginning of my thesis work. Thank you for always being willing to share your great knowledge of physics and engineering. Besides, your practical approach to problem-solving, energy, and strength of character are an inspiration for me. Lastly, this thesis would not have been submitted without your help, for that, I will always be grateful.

Titus Franz, it was a pleasure to work with you on the Rydberg spins experiment. You are a great colleague, with whom I learned a lot. Thank you also for supporting me with my thesis after I left Heidelberg.

It was also a enjoyed sharing the laboratory with **Dr. Miguel Ferreira Cao** and **Dr. Vladislav Gavryusev** for the first part of my doctoral research. I really appreciate the many nice moments we had together.

During this time I had the opportunity of working with **Dr. Adrien Signoles**, who showed me how to operate the Rydberg experiment. I remember, learning a lot from our discussions during the experimental runs, and I would like to thank you for that.

Thank you also to my postdocs **Dr. Clément Hainaut**, for the many conversations about physics and life in general, and for the eventual happy hour at the Mensa, and to **Dr. Nithiwadee Thaicharoen**, for your energetic and positive attitude that elevated the mood of the whole team. It was great working with both of you.

A special thanks goes to my laboratory colleagues **André Salzinger**, **Sebastian Geier**, **David Grimshandl**, **Henrik Zahn**, **Alexander Müller**, and **Annika Tebben**, I keep good memories of all of you. It was a pleasure to work with such nice, talented, and smart people. André and Sebastian, thank you also for reviewing my thesis.

Ao meu amigo **Prof. Dr. André Luiz de Oliveira**, muito obrigado pelo apoio e pelos bons momentos em Heidelberg.

Let me also thank **Mrs. Claudia Krämer** for your support during my time in Heidelberg.

Por último, quero deixar os meus agradecimentos a minha **família**, que me deu fundamental apoio durante esse desafio. Primeiramente agradeço a minha amada esposa **Nathalia**, que compartilhou comigo essa jornada. Aos meus pais **Leonice** e **Tadeu**, obrigado pelo incentivo e ajuda durante minha tese. A minha irmã **Mariana**, meu cunhado **Aaron**, e meus sobrinhos **Sophia** e **Lucas**. A minha tia **Maria Lúcia**, que sempre torceu pro mim e me deu força para terminar o doutorado. E finalmente, aos meus amados filhos **Gabriel** e **Murilo**.